New approach to evaluate satellite derived XCO₂ over oceans by integrating ship and aircraft observations

Astrid Müller[1], Hiroshi Tanimoto[1], Takafumi Sugita[1], Toshinobu Machida[1], Shin-ichiro Nakaoka[1], Prabir K. Patra[2], Joshua Laughner[3], David Crisp[4]

1 National Institute for Environmental Studies, Tsukuba, Japan
2 Japan Agency for Marine-Earth Science and Technology, Yokohama, Japan
3 California Institute of Technology, Pasadena, CA, USA
4 Jet Propulsion Laboratory/California Institute of Technology, Pasadena, CA, USA

Correspondence and request for material should be addressed to:
Hiroshi Tanimoto (tanimoto@nies.go.jp), Astrid Müller (mueller.astrid@nies.go.jp)

Abstract. Satellite observations provide spatially-resolved global estimates of column-averaged mixing ratios of CO_2 (XCO_2) over the Earth's surface. The accuracy of these datasets can be validated against reliable standards in some areas, but other areas remain inaccessible. To date, limited reference data over oceans hinders successful uncertainty quantification or bias correction efforts, and precludes reliable conclusions about changes in the carbon cycle in some regions. Here, we propose a new approach to analyze and evaluate seasonal, interannual and latitudinal variations of XCO_2 over oceans by integrating cargo-ship (SOOP, Ship Of Opportunity) and commercial aircraft (CONTRAIL, Comprehensive Observation Network for Trace gases by Airliner) observations with the aid of state-of-the art atmospheric chemistry-transport model calculations. The consistency of the "observation-based column-averaged CO_2" dataset (obs. XCO_2) with satellite estimates was analyzed over the Western Pacific between 2014 and 2017, and its utility as reference dataset evaluated. Our results demonstrate that the new dataset accurately captures seasonal and interannual variations of CO_2. Retrievals of XCO_2 over the ocean from GOSAT (Greenhouse gases observing satellite: NIES v02.75, National Institute for Environmental Studies; ACOS v7.3, Atmospheric CO_2 Observation from Space) and OCO-2 (Orbiting Carbon Observatory, v9r) observations show a negative bias of about 1 parts per million (ppm) in northern midlatitudes, which was attributed to measurement uncertainties of the satellite observations. The NIES retrieval had higher consistency with obs. XCO_2 at midlatitudes as compared to the other retrievals. At low latitudes, it shows many fewer valid data and high scatter, such that ACOS and OCO-2 appear to provide a better representation of the carbon cycle. At different times, the seasonal cycles of all three retrievals show positive phase shifts of one month relative to the observation-based data. The study indicates that even if the retrievals complement each other, remaining uncertainties limit the accurate interpretation of spatiotemporal changes in CO_2 fluxes. A continuous long-term XCO_2 dataset with wide latitudinal coverage based on the new approach has a great potential as a robust reference dataset for XCO_2 and can help to better understand changes in the carbon cycle in response to climate change using satellite observations.

1 Introduction

35 Efforts to control the accelerated increase of carbon dioxide (CO_2) in the atmosphere became a serious international task in the last decades. CO_2 is the most important anthropogenic greenhouse gas (GHG). Since the beginning of the Industrial Era in the 1750s, fossil fuel combustion and other human activities have increased the atmospheric concentration of CO_2 from approximately 277 ppm to more than 410 ppm in 2020 (Dlugokencky, E. and Tans P.: Trends in Atmospheric Carbon Dioxide, NOAA/GML; www.esrl.noaa.gov/gmd/ccgg/trends/, last access: 7 January 2021). On average, less than half of the

40 anthropogenic CO_2 emitted each year stays in the atmosphere, as the ocean and land each capture approximately one-fourth (Friedlingstein et al., 2019). Seasonal changes in CO_2 uptake and release alter the fraction of atmospheric CO_2 substantially and lead to year-to-year variations, which are not yet fully understood (e.g. Friedlingstein et al., 2019; Intergovernmental Panel on Climate Change (IPCC), 2013). As the carbon cycle responds to a changing climate, a comprehensive understanding of changes in CO_2 sources and sinks is crucial to the implementation of effective strategies for reducing global warming.

45 In situ measurements from ground-based networks and aircraft campaigns provide precise information on local CO_2 concentrations. There are now more than 100 surface measurement sites around the globe, but most are located on land in North America and Europe, and some in the East Asia and Oceania, and few in other continents (e.g., Crowell et al., 2019; Hakkarainen et al., 2019). Very few sites are located over the open oceans, even though 70% of the Earth's surface is covered by water and the ocean is a key element of the global carbon cycle. The uneven distribution and limited spatial coverage of in

50 situ measurements makes it difficult to infer CO_2 fluxes between the surface and the atmosphere on regional to global scales at high accuracy (Canadell et al., 2011; Chevallier et al., 2010, 2011). Space-based remote sensing measurements are complementing in situ observations. Their high spatial and temporal coverage allows observation of changes in atmospheric CO_2 mixing ratios even in regions with poor in situ coverage (Baker et al., 2010, Crisp et al., 2012). By collecting high resolution spectra of near infrared (NIR) and shortwave infrared (SWIR) solar radiation reflected from the Earth's surface,

55 satellite observations can yield estimates of the total atmospheric column of CO_2. These observations are most sensitive to the lower troposphere where CO_2 is most variable (Patra et al., 2003) and therefore, are able to improve the knowledge on local CO_2 emission and sinks (Connor et al., 2008).

Japan's Greenhouse gases Observing Satellite (GOSAT), and the second NASA's (National Aeronautics and Space Administration) Orbiting Carbon Observatory (OCO-2) are dedicated to inferring the concentration of GHGs from high-

60 resolution spectra at NIR and SWIR wavelengths. Since their launches in 2009 and 2014, GOSAT and OCO-2 have successfully provided global datasets of column-averaged mixing ratios of CO_2 (XCO_2). In 2018, GOSAT-2 was launched, aiming to improve the measurement precision and to overcome anomalies of the spectrometer on board GOSAT (Nakajima et al., 2017). The launch of OCO-3 followed in 2019. Since 2009, NASA's Atmospheric CO_2 Observation from Space (ACOS) and GOSAT team work closely together on the analysis of GOSAT observations (Crisp et al., 2012; O'Dell et al., 2012).

65   Comparisons of XCO_2 generated by the GOSAT team of the National Institute for Environmental Studies (NIES) (e.g., Yoshida et al., 2013) with that of the ACOS retrieval algorithm are aimed to improve the accuracy of the estimated XCO_2.

    Variations in the CO_2 concentration associated with surface sources and sinks are typically not larger than 1 ppm (0.25%), and annual and seasonal variations of XCO_2 are small compared to the mean abundance in the atmosphere (Crisp et al., 2012; Miller et al., 2007). Therefore, a precision of 1–2 ppm for CO_2 satellite retrievals is needed (Crisp et al., 2012). Any
70 uncharacterized systematic errors in the retrieval affect the accuracy of XCO_2 and limit its utility for carbon cycle studies (Basu et al., 2013). Therefore, extensive validation of satellite XCO_2 has been performed, mainly against data of the Total Carbon Column Observing Network (TCCON) (Wunch et al., 2011), which is a network of ground-based Fourier transform infrared (FTIR) spectrometers. However, TCCON sites are land based and very limited number of sites observe the atmosphere over open oceans, which are defined as the ocean area outside the coastal region. Between the GOSAT NIES soundings over the
75 ocean and TCCON sites near the ocean, a bias of -1.09 ± 2.27 ppm was found (Morino et al., 2020). Negative XCO_2 anomalies north and south of the equator are observed in the OCO-2 retrieval over the Pacific Ocean (Hakkarainen et al., 2019). In combination with surface measurements, vertical profiles of CO_2 obtained by aircraft can constrain XCO_2 but are very limited (e.g., Frankenberg et al., 2016; Inoue et al., 2013; Wofsy, 2011; Wofsy et al., 2018). Inoue et al. (2013) found a bias as large as -1.8 to -2.3 ppm between aircraft-based XCO_2 and that from GOSAT NIES at the Pacific Ocean. Comparisons of ACOS
80 GOSAT XCO_2 estimates to those from HIAPER Pole-to-Pole Observations (HIPPO) campaigns (Frankenberg et al., 2016) show lower bias (-0.06 ppm) and standard deviation (0.45 ppm). More recent comparisons of OCO-2 XCO_2 estimates to in situ measurements from the NASA Atmospheric Tomography Mission reveals a systematic bias of -0.7 ppm over the tropical Pacific, that is also seen in the data at Burgos, a TCCON station in that region (Kulawik et al., 2019; Velazco et al., 2017). Limited reference data in the tropical and high latitudinal oceans are the reason for major uncertainties in satellite retrievals
85 over these regions. Therefore, variations in XCO_2 over ocean sites cannot be reliably captured, but this is necessary for modeling the future climate (e.g., Crowell et al., 2019).

    We propose a new approach to analyze and evaluate seasonal, interannual and latitudinal variations of satellite derived XCO_2 by integrating cargo-ship and commercial aircraft observations. We use long-term datasets of the dry air mole fraction of CO_2 from Japan's CONTRAIL (Comprehensive Observation Network for Trace gases by Airliner) and SOOP (Ship Of
90 Opportunity) project which cover wide latitudinal and longitudinal regions of the Pacific and South China Sea. Together with state-of-the art atmospheric chemistry-transport model calculations (Patra et al., 2018), we calculate observation-based XCO_2. The consistency of the spatiotemporal variation of the ship-aircraft based XCO_2 with satellite estimates from OCO-2, and two GOSAT retrievals (NIES, ACOS) is analyzed, and its utility as long-term reference dataset evaluated.

2 Observational Data

2.1 Aircraft

Japan's Comprehensive Observation Network for Trace gases by Airliner, CONTRAIL, uses commercial aircraft flying between Japan and Europe, Asia, Australia, Hawaii and North America to continuously measure atmospheric CO_2 since 2005. In cooperation with Japan Airlines (JAL), the Continuous CO_2 Measuring Equipment (CME) is installed in the forward cargo compartment on 777-200ER or 777-300ER aircraft (Machida et al., 2008; Umezawa et al., 2018). The CME measures the CO_2 dry mole fraction using a non-dispersive infrared gas analyzer (NDIR; LI-840, LI-COR Biogeosciences). Air samples are taken from the air conditioning system of the aircraft. Before the samples are analyzed by the NDIR, a diaphragm pump draws the samples through a drier tube packed with CO_2-saturated magnesium perchlorate to remove water vapor. The flow rate and absolute pressure in the NDIR are kept constant by a mass flow controller and auto pressure controller, respectively.

Two standard gases are introduced into the NDIR every 14 minutes (min) during the ascent and decent portions of the flight and every 62 min during the cruise at 8-12 km height (Machida et al., 2008; Umezawa et al., 2018). Forty seconds (s) after the switch from standard gas to air sample, data are collected as averages of 10 s during the ascent and decent, and 1 min averages during the cruise (~ 15 km horizontal distance). Data of each 10 s and 1 min period are rejected if the standard deviation exceeds 3 ppm (Umezawa et al., 2018). The analytical uncertainty of the CME is 0.2 ppm, which was estimated from the comparison with occasional flask sampling, using an automatic air sampling equipment (Matsueda et al., 2008).

In this study, we used CME data v2019.1.0 from flights between Narita and Sydney over the Western Pacific Ocean between 2014 and 2017. Only those data which were obtained below the tropopause height during the cruise at around 11 km altitude are used. To define the tropopause height, we used the blended tropopause pressure (TROPPB), which is explained in detail in **section 3.2**. Data of the lower stratosphere were only occasionally obtained. We screened out those data in order to have a consistent methodology for constructing CO_2 profiles as explained in **section 3.2**.

2.2 Ship

Commercial cargo Ships of Opportunity (SOOP) have been collecting samples of atmospheric CO_2 on cruises since 2001 between Japan and North America, since 2005 between Japan and Australia and New Zealand, and since 2007, between Japan and South East Asia. In this study, we used data collected by the cargo ship Trans Future 5 (Toyofuji Shipping Co., Ltd.), which sails between Japan, Australia, and New Zealand. The dry air mole fraction of CO_2 is measured by a NDIR (MOG-701, Kimoto Electric Co.) every 10 s with an accuracy of 0.1 ppm. The NDIR is installed on top of the bridge at approximately 30 m above sea level (Yamagishi et al., 2012). Samples are drawn into the NDIR through a tube, whose inlet is placed at a location which is not affected by smoke of the ship. Calibration is done every 6 hours by introducing four CO_2 standards (360, 380, 400, 420 ppm, Taiyo Nippon Sanso Corporation, Japan).

2.3 Satellite

125   Japan's GOSAT launched in 2009, and NASA's OCO-2 launched in 2014, were developed to characterize the variability of the atmospheric CO_2 fraction at regional scales over the globe. Both the OCO-2 grating spectrometer and the Thermal And Near infrared Sensor for carbon Observations – Fourier Transform Spectrometer (TANSO-FTS) instrument on board GOSAT measure the reflected sunlight in three shortwave infrared (SWIR) channels: at around 0.764 μm, which contains significant O_2 absorption, at 1.61 μm which contains a weak CO_2 absorption band, and at 2.06 μm, containing a strong CO_2 absorption

130   band (Crisp et al., 2017; Kuze et al., 2009). By measuring the amount of light absorbed by CO_2 and O_2, the column average CO_2 dry air mole fraction (XCO_2) is estimated by taking ratio of the total column amounts of CO_2 and the total column of dry air (O'Dell et al., 2012, 2018; Wunch et al., 2011; Yoshida et al., 2011, 2013).

When the launch system failed for the first OCO in 2009, the ACOS team modified the retrieval algorithm originally developed for OCO to allow GOSAT retrievals (O'Dell et al., 2012). In this study, we selected level 2 XCO_2 data in sun-glint mode from

135   the NIES v02.75 (Yoshida et al., 2013), ACOS v7.3, and OCO-2 v9r retrieval algorithm, all of which were bias corrected. NIES v02.75 uses only cloud-free scenes. For ACOS and OCO-2, we chose data with a good quality flag (quality flag = 0), which is provided by each algorithm. The ACOS data processing is ongoing and data of version 7.3 are available until June 2016. At the time of writing the manuscript, ACOS version 9 was released. This version is based on a newer version of the GOSAT Level 1 product, which includes extended sun-glint data. Furthermore, OCO-2 version 10 was released. An initial

140   comparison between ACOS v7.3 and v9, and between OCO-2 v9r and v10 is included in the Appendix A (Figs. A1 and A2) and section 5 Conclusions. In the following, we refer to data obtained by OCO-2 v9r and GOSAT using the retrieval algorithm from NIES v02.75 and ACOS v7.3 simply as "OCO-2", "NIES", and "ACOS", respectively.

3 Methodology

3.1 Data selection

145   In order to compare data of all satellite retrievals, we chose the time period from 2014 to 2017, when both GOSAT (NIES, ACOS) and OCO-2 XCO_2 products are available. Over the Western Pacific between 40° N and 30° S, we made 10° latitude by 20° longitude wide boxes around the ship and aircraft data in order to obtain enough co-located data for the seasonal and interannual comparison with satellite retrievals **(Fig. 1)**. Within these boxes, no significant latitudinal and longitudinal variation of the CO_2 mixing ratio is expected (Sawa et al., 2012). Results of the MIROC4 (Model for Interdisciplinary Research On

150   Climate Earth System, version 4.0)-based Atmospheric Chemistry Transport model (ACTM) were obtained for each hourly averaged location of the aircraft. The details of the MIROC4-ACTM are described in Patra et al. (2018). In short, the MIROC4-ACTM uses a hybrid vertical coordinate to resolve gravity wave propagation in the stratosphere, where at least 30 model layers reside. The hybrid coordinate transitions from sigma coordinates at the surface to pressure levels around the tropopause. In total, 67 vertical layers are used between the Earth's surface and 0.0128 hPa. The MIROC4-ACTM has a horizontal resolution

155   of triangular 42 truncation (T42) which corresponds to approximately 2.8° longitude by 2.8° latitude. The ACTMs are nudged with the Japanese 55-year Reanalysis (JRA-55; Kobayashi et al., 2015) for horizontal winds and temperature at Newtonian relaxation times of 1-hour and 5-hours, respectively. Nudging is performed for all the model layers from 2 to 60. A high accuracy of the MIROC4-ACTM is indicated by the agreement of simulated "age of air", which is a diagnostic for atmospheric transport, with that expected from measured sulphur hexafluoride (SF_6) and CO_2 in the troposphere and stratosphere,

160   respectively (Patra et al., 2018). All data obtained over land are excluded in the current study. For the analysis of the seasonal and interannual variation of CO_2, we chose the monthly averages of the satellite, in situ, and model datasets. In this study, we focus on the results of the latitude ranges 20° N–30° N, 0° N–10° N, and 20° S–10° S, as representative for the northern midlatitude, the equator region, and southern latitudes, respectively.
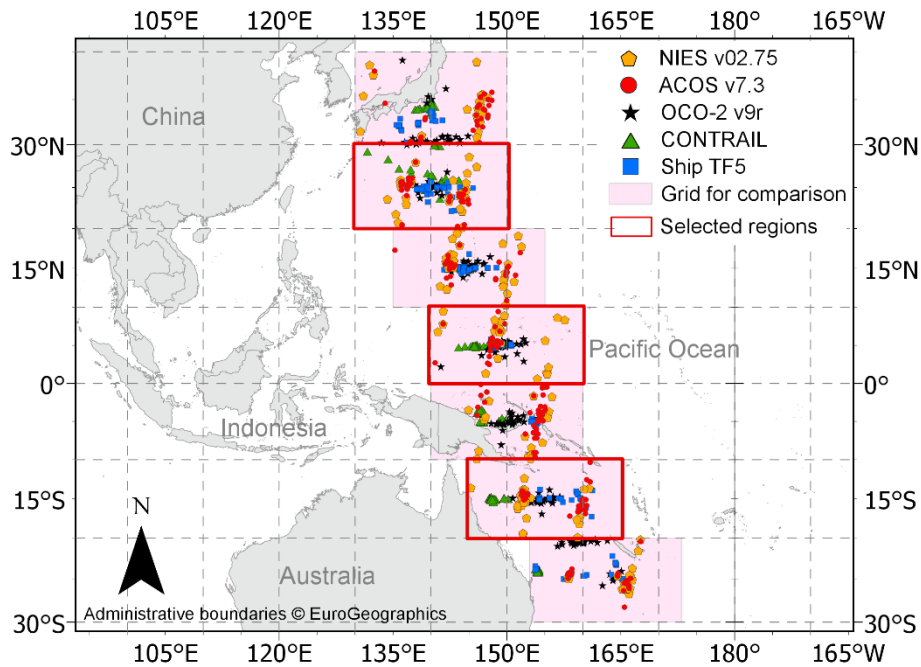
165   **Figure 1.** Location of monthly averaged data of CO_2 from aircraft (CONTRAIL, green triangle), ship (Trans Future 5 - TF5, blue squares), the satellite retrievals from NIES (yellow diamonds), ACOS (red circles), and OCO-2 (black stars) between 2014 and 2017. Selected regions within 10° latitude by 20° longitude boxes are shown in red frames. Administrative boundaries © EuroGeographics.

3.2 Observation-based CO₂ profile construction and XCO₂ calculation

170   **Figure 2** shows how atmospheric CO_2 profiles are constructed with the aid of ship and aircraft data in order to derive column averaged mixing ratios of CO_2. Ship data are extrapolated vertically to ~850 hPa, which corresponds to the 3rd and 4th pressure level of NIES and ACOS, respectively, counted from the surface. We chose this cut off as it represents the boundary layer

above sea level in which most of the rapid variation of CO_2 occur. Previous balloon and aircraft measurements by the HIPPO campaign over the Tropical Eastern and Western Pacific showed stronger CO_2 variation of about 1 to 2 ppm within the first 2 km above sea level. Above this level, the CO_2 mixing ratios were rather stable or kept changing linearly up to about the tropopause height (Frankenberg et al., 2016; Inai et al., 2018). To account for that variation within the boundary layer, we added a ±2 ppm uncertainty to the CO_2 estimates at ~850 hPa. Aircraft data from the cruise portion of the flight, which is usually between 380 and 200 hPa, are selected. These aircraft data are extrapolated down to the lower cruising height limit at 380 hPa, and at 30° N–40° N at 400 hPa. Furthermore, the aircraft data is also extrapolated upwards to the blended tropopause pressure (TROPPB).

The TROPPB is defined as a combination of a thermal tropopause- and dynamic tropopause pressure (Wilcox et al., 2012). The TROPPB data are extracted from GEOS-FP (Goddard Earth Observing System – forward processing) meteorology data using the python suite "ginput" version 1.0.6 (Laughner et al., 2021). Ginput was developed to generate a priori vertical mixing ratios of chemical species (e.g., CO_2, CO, CH_4, N_2O) for the open source TCCON retrieval algorithm, GGG2020 (Laughner et al., in prep). The TROPPB was calculated every 3 hours on the 5th, 15th, and 25th of each month for each centre location of the 10° latitude by 20° longitude boxes. Between 2014 and 2017, the highest monthly variation was found at 20° N–30° N with a standard deviation ranging from 0 to 24 hPa (0.02 to 23.77 hPa) and an average standard deviation of 10 ± 5 hPa. The maximum difference of 24 hPa at the level of the TROPPB corresponds to difference in the altitude of 1 to 2 km. Assuming a straight profile between the extrapolated aircraft and ship data, we linearly interpolate in both pressure and volume mixing ratio.
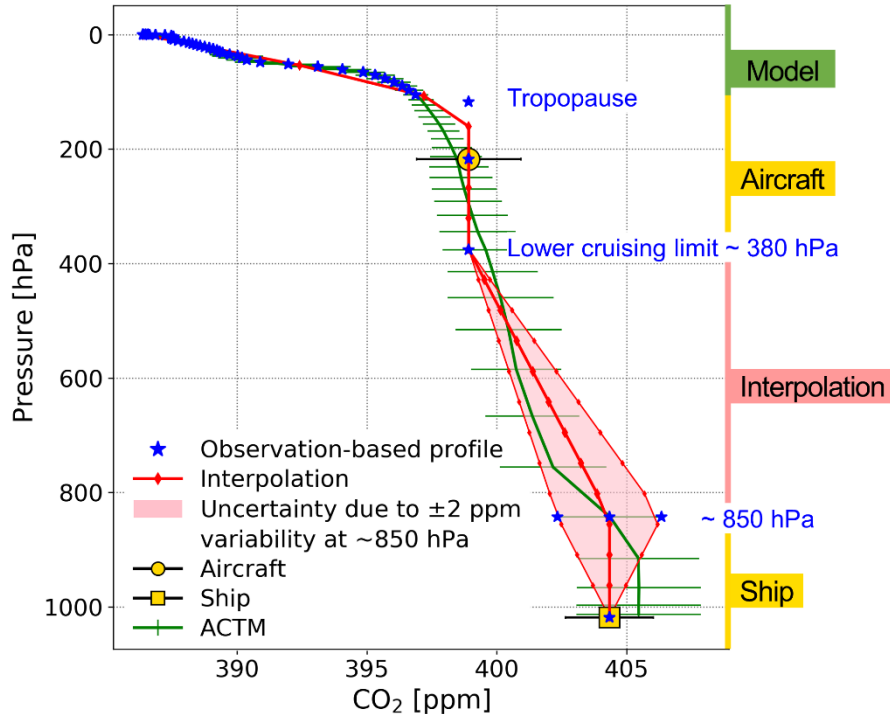
Figure 2. Construction of the observation-based CO_2 profile (blue) obtained by using ship (SOOP) and aircraft (CONTRAIL) data (yellow) together with the results of the ACTM (green), and the interpolation (red). The example is obtained at the latitude 20° N–30° N, March 2014.

195   Total column observations in the atmosphere consists of up to 40% air in the stratosphere (Patra et al., 2018). To account for the stratospheric partial column, we used results of the MIROC4-ACTM (Patra et al., 2018) above the TROPPB (**Fig. 2**) instead of the results from ginput. First, by using the MIROC4-ACTM, our method is fully independent of TCCON, which is important for using our methodology as a complement to TCCON to evaluate satellite retrievals. Second, the MIROC4-ACTM uses realistic flux and transport simulations and is one of the best validated stratospheric models at present.

200   To calculate the XCO_2 that the satellite would have seen given the CO_2 profile constructed from in situ data, we first interpolate these profiles onto the corresponding monthly averaged pressure grid of the ACOS and NIES retrievals, then we use Eq. (15) of Connor et al. (2008):

$$X^m_{CO2} = X^a_{CO2} + \sum_j h_j\, a_{co2,j}\, (x_m - x_a)_j \tag{1}$$

Here, X^m_{CO2} is the total column XCO_2 that the satellite would report if it observed the constructed CO_2 profile x_m. We refer to

205   X^m_{CO2} as "observation-based XCO_2" (obs. XCO_2) in the following. x_m is the observation-based CO_2 profile (as a true profile). Extracted from the corresponding satellite retrievals, X^a_{CO2} is the a-priori XCO_2 of OCO-2, NIES, and ACOS, respectively, h_j

the pressure weighting function, which is the change of atmospheric transmittance with respect to the pressure, $a_{CO2,j}$ is the column averaging kernel, which represents the sensitivity profile to the total column amount, and x_a the a priori CO_2 profile. Comparison between monthly averages of the calculated obs. XCO_2 using $X_{CO2}^a, h_j, a_{CO2,j},$ and x_a from the NIES and ACOS files showed agreement within 0.1 ± 0.1 ppm. Because the ACOS retrieval provides a higher number of valid data, we used the pressure levels and parameters from ACOS as representative for the calculation. After May 2016, we use the pressure grid and parameters from NIES due to the temporal limit of the ACOS v7.3 product.

It is noted that in our approach to obtain obs. XCO_2, the usage of model results above the TROPPB introduces little bias for two reasons. First, the CO_2 mixing ratio at these pressure levels varies much less than that in the middle and lower troposphere since there are no significant CO_2 sources and sinks in the stratosphere. Second, as mentioned earlier, the MIROC4-ACTM is among the best validated stratospheric models using high altitude balloon-borne measurements of SF_6 and CO_2-age-of-air (Patra et al., 2018), and in the upper troposphere and lower stratosphere using CONTRAIL observations (Bisht et al., 2021). Furthermore, in a sensitivity test, we compared XCO_2 derived from CO_2 profiles using the MIROC4-ACTM with that where the part of the CO_2 profile above the TROPPB was filled in by extrapolating the aircraft data up to 0.0128 hPa. The difference in XCO_2 was only 0.2 ± 0.1 ppm on average.

4 Result and Discussion

4.1 Spatiotemporal variation of CO_2 seen by ship, aircraft, and satellite

Figure 3a-c presents the temporal variation of monthly average CO_2 mixing ratios obtained by ship and aircraft in three representative latitude ranges, namely the northern midlatitudes (20° N–30° N), the equator region (0° N–10° N), and southern latitudes (20° S–10° S). Ship and aircraft data refer to lower and upper tropospheric CO_2 mixing ratios. The largest seasonal cycle of the CO_2 mixing ratio is seen in the northern hemisphere (NH) at 20° N–30° N. Average CO_2 mixing ratios of 402.9 ± 3.6 ppm and 401.2 ± 3.1 ppm at lower and upper troposphere, exceeded that from south of the equator by 4.5 ppm and 1.5 ppm, respectively. Maxima occur in April to May at sea level, which is approximately 1 month earlier than in the upper troposphere (May to June). Minima seen in autumn show a greater temporal variability in the lower troposphere (August to October) than at about 10 km height (September). At 20° N–30° N, the peak-to-trough amplitudes of the seasonal cycles at sea level is 8.5 ± 0.9 ppm, and is ~2 ppm larger than the amplitudes in the upper troposphere (6.5 ± 0.6 ppm). Amplitudes decrease with latitude, showing similar values of about 4 ppm at the equator. In the southern hemisphere (SH), the amplitudes approach 0 at sea level **(Fig. 3c)**. In contrast, the upper troposphere shows two small peaks, one in June and one in November/December in 2014 and 2015, and additionally in April 2016. Seasonal cycles and decreasing amplitudes in the upper troposphere from North to South (7 ppm to 4 ppm) are similar to that observed by Matsueda et al. (2008). They found a decrease from 6 ppm at 30° N to 3 ppm at the equator over the same region between 2005 to 2007 using aircraft based flask samples. At sea level, seasonal cycle amplitudes that decrease from about 8 ppm at 20° N–30° N to 3 ppm at the equator were reported by the global

sampling network of the National Oceanic and Atmospheric Administration's Climate Monitoring and Diagnostics Laboratory (NOAA/CMDL) (Conway et al., 1994). The current observed characteristics are consistent with the previous long-term studies.
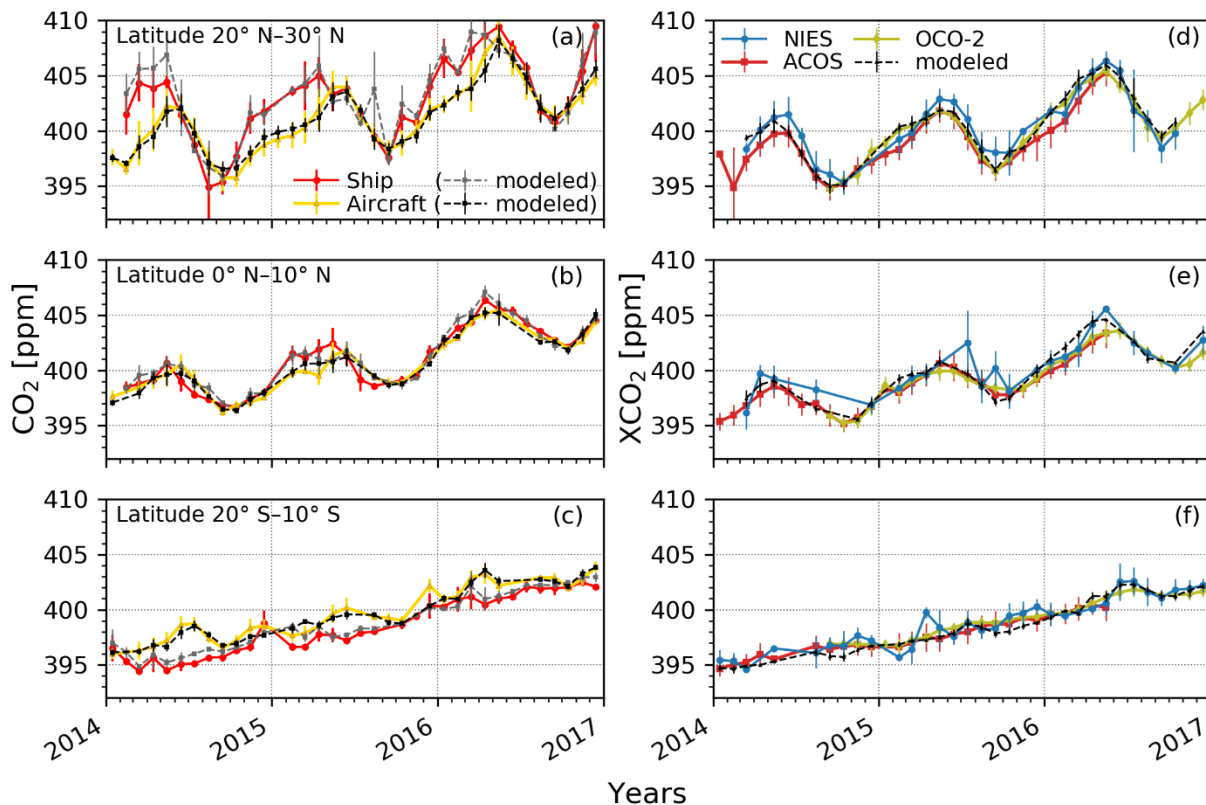
240

Figure 3. Temporal variation of the monthly average CO_2 mixing ratio obtained by ship (red) and aircraft (yellow) (left column), and the column averaged mixing ratios (XCO_2) from the NIES (blue), ACOS (red), and OCO-2 (olive) (right column) in three representative latitude ranges for the northern midlatitudes a) and d), the equator region b) and e), and southern latitudes c) and f). Results of the ACTM are shown as dashed lines. Error bars represent the standard deviation of the monthly averages.

245

As the NH transitions from winter to spring, **Fig. 3a** reveals that the CO_2 mixing ratio increases rapidly at the surface, but only moderately at the upper troposphere, which results in a difference of up to 4 ppm. In 2014 and 2015, upper tropospheric peak values show a delay of 1 month, which is not seen in 2016, likely due to year-to-year variations. Similar observation have been made previously over the northern Pacific (Miyazaki et al., 2008; Nakazawa et al., 1991) and attributed to the response of the

250 terrestrial carbon metabolism of the NH (China, Korea, Japan) and predominant northwesterly airmass transport (Umezawa et al., 2018). Specifically, low net primary productivity (NPP) and leaf litter decomposition in autumn to winter is linked to a net carbon release from the terrestrial ecosystem and subsequent increase in the CO_2 mixing ratio at the lower troposphere, which persists until spring. Vertical mixing mitigates the altitude dependent CO_2 gradient with a time offset of about 5 months. In spring to summer, high NPP rates substantially removes CO_2 from the atmosphere. At that season, strong convection,

associated with significant uplift of low-CO_2 air masses, results in a well-mixed troposphere (Miyazaki et al., 2008; Nakazawa et al., 1991; Niwa et al., 2011). The flux footprints on upper tropospheric CO_2 is generally much wider compared to that near the surface at all latitudes, resulting in a smoother vertical gradients and smaller seasonal cycle amplitudes at higher altitudes.

Figure 3d-f presents the temporal variation of column averaged mixing ratios of CO_2 (XCO_2) retrieved by NIES, ACOS, and OCO-2. The number of valid bias corrected XCO_2 retrievals by NIES are less than 25 % of that by ACOS with good quality flag. Seasonal patterns of all retrievals were similar in the NH, showing peaks in late spring/early summer (May to June), and minima in autumn (September to October). While peaks of XCO_2 by NIES are higher by 1 to 3 ppm, ACOS and OCO-2 values agree within 1 ppm (**Figs. 3d and 3e**). The largest amplitudes of ACOS and OCO-2 at 20° N–30° N (5 to 6 ppm) are approximately 2 ppm smaller than those of NIES (6 to 8 ppm). Southwards, the strong seasonal cycle decreases, and disappears in the SH, similar to observations made by in situ measurements at sea level. The NIES XCO_2 product shows substantial scatter and limited valid data each month at lower latitudes, unlike ACOS and OCO-2 (**Figs. 3e and 3f**). Differences in retrieval algorithms can explain discrepancies in the XCO_2 (Reuter et al., 2013), while the reduced number of data points of NIES are likely due to stricter quality filters. The results imply that seasonal variations of CO_2 at lower latitudes are better represented by the ACOS/OCO-2 retrieval algorithm.

Table 1. Root-mean-square error (RMSE), and average difference and standard deviation between the retrievals from aircraft, ship, satellite and the corresponding results from the ACTM at different latitude ranges between 2014 and 2017.

			RMSE		
Latitude	**Aircraft**	**Ship**	**NIES**	**ACOS**	**OCO-2**
20° N–30° N	0.54	1.26	0.93	1.09	0.44
0° N–10° N	0.44	0.68	1.14	0.93	0.93
20° S–10° S	0.55	0.63	0.86	0.54	0.56
		Difference measured in situ or/satellite XCO_2 − ACTM (ppm)			
Latitude	**Aircraft**	**Ship**	**NIES**	**ACOS**	**OCO-2**
20° N–30° N	0.00 ± 0.54	-0.41 ± 1.19	0.16 ± 0.92	-0.81 ± 0.72	-0.30 ± 0.32
0° N–10° N	0.01 ± 0.44	-0.20 ± 0.65	0.17 ± 1.13	-0.58 ± 0.72	-0.51 ± 0.78
20° S–10° S	0.13 ± 0.54	-0.40 ± 0.48	0.33 ± 0.80	0.15 ± 0.52	0.20 ± 0.52

Figure 3 also presents the simulated XCO_2, sea level CO_2 mixing ratios, and upper troposphere CO_2 mixing ratios, calculated by the MIROC4-ACTM. Best agreement is found between the model results in the upper troposphere and the aircraft observations (RMSE 0.51 ± 0.05, average difference 0.05 ± 0.06) (**Table 1**). The largest discrepancy to the model results occur for the ship observations at northern midlatitudes (RMSE 1.26, difference 0.41 ± 1.19), likely due to the large gradients and variations of CO_2 concentrations typically found at this latitude range at sea level. The coarse horizontal resolution of the

model is not adequate to represent observations near source regions. The RMSE of the difference between satellite XCO_2 and the MIROC4-ACTM ranges from 0.44 to 1.14, which may result both from the higher uncertainties of the simulations at sea level, and the uncertainties in the satellite retrievals. OCO-2 v9r shows systematically higher RMSE around the equator at 0° N–10° N, relative to the 20° N–30° N and 10° S–20° S region.

4.2 Latitudinal variations of CO_2 seen by ship, aircraft, and satellite

Figure 4a-c displays the latitudinal distribution of the CO_2 mixing ratio of ship and aircraft for three selected months in 2015, which are representative for different latitudinal CO_2 gradients in the troposphere. From North towards the equator, the negative tropospheric CO_2 gradient decreases rapidly, especially in spring (March) and autumn (October) (**Figs. 4a and 4c**). Around the equator, ship and aircraft mixing ratios agree within 0.2 ± 0.8 ppm. In the SH, the gradient is reversed, showing upper tropospheric CO_2 mixing ratio to be larger by 1.4 ± 0.9 ppm, especially during NH spring to summer (**Fig. 3c, Fig. 4b**). Previous model studies, which included aircraft observations, explain the atmospheric CO_2 characteristics south of the equator by meridional transport processes (Miyazaki et al., 2008; Niwa et al., 2011). Our current ACTM forward simulations reveal in particular that CO_2, which is strongly emitted during winter to spring (December to May) over NH land, causes a strong meridional CO_2 gradient at sea level, and the CO_2 rich air is transported towards the equator (**Fig. A2**). In NH summer (June to August), the meridional gradient is substantially weakened due to the seasonal CO_2 sink at northern midlatitudes (**Fig. 4b, Figs. A2f-h**). At the upper troposphere, meridional gradients are absent during autumn (September-November) (**Fig. 4c, Figs. A2i-k**) and gradients are weak in winter (December to February) (**Figs. A2l-b**), but increase towards summer due to vertical mixing of CO_2 rich air from the surface at northern midlatitudes (**Fig. 4a, Figs. A2c-e**). Near the equator, uplift by convection increase the CO_2 mixing ratio in the middle and upper troposphere in all seasons. In the SH, strong meridional transport from the NH to the SH occurs only from late spring to early summer in the upper troposphere during which time the CO_2 mixing ratio in the upper troposphere exceeds that at the sea-surface (**Fig. 4b**). Furthermore, CO_2 uptake by the Southern Pacific and southern hemispheric land vegetation decrease CO_2 at sea level. The current in situ observations confirm the inter-hemispheric transport mechanism of CO_2.
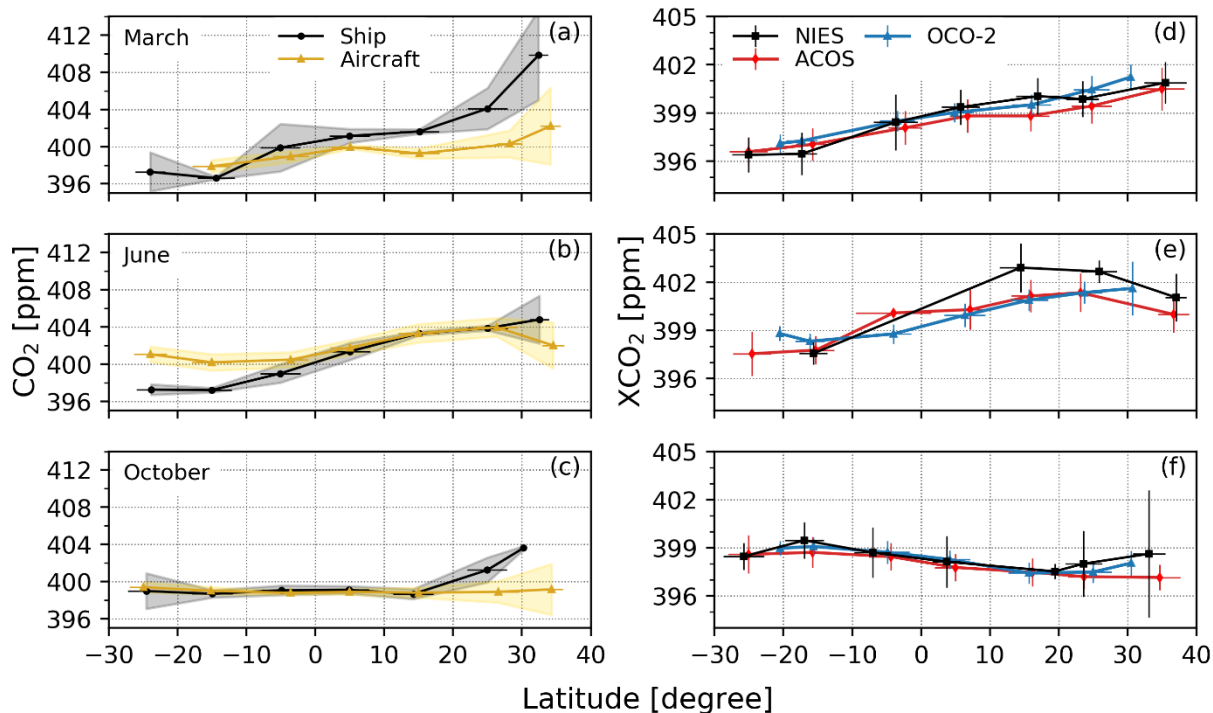
Figure 4. Latitudinal distribution of the CO$_2$ mixing ratio obtained by ship (black) and aircraft (yellow) (left column), and of XCO$_2$ obtained by NIES (black), ACOS (red), and OCO-2 (blue) (right column) for three selected months in 2015, which are representative for different latitudinal CO$_2$ gradients in the troposphere: March a) and d), June b) and e), and October c) and f). Shaded areas are the standard deviation of the monthly average CO$_2$ mixing ratios. Error bars show the standard deviation of the monthly averaged XCO$_2$, and of the location within each latitude box.

Figure 4d-f shows the latitudinal distribution of XCO$_2$ retrieved by NIES, ACOS, and OCO-2. In spring, maximum values appear in the NH and minima in the SH (**Fig. 4d**). In autumn, the locations of the maxima and minima are reversed between NH and SH (**Fig. 4f**). In summer (June), the maxima occur at 10° N–20° N (**Fig. 4e**), which is the result of substantial carbon removal by high NPP at higher latitudes (30° N–40° N) as described above. At that transition point, XCO$_2$ of NIES exceeds that of ACOS and OCO-2 by about 2 ppm. The in situ and satellite observations reveal the complex CO$_2$ fluxes and transport processes. The results demonstrate that measuring upper and lower tropospheric CO$_2$ mixing ratios simultaneously is important to better understand CO$_2$ fluxes, which is necessary to further improve atmospheric chemistry transport models. The consistency of the satellite XCO$_2$ with in situ observations will be evaluated by comparison with the corresponding obs. XCO$_2$ values in the following section.

4.3 Evaluation of seasonal and interannual changes of satellite XCO$_2$ by combined ship and aircraft observations

Figure 5a-c shows the temporal variation of the satellite and obs. XCO$_2$, and the difference between obs. and satellite XCO$_2$ in **Figs. 5d-f**. The uncertainties of the obs. XCO$_2$ dataset are estimated to be 0.62 ± 0.01 ppm on average, which is derived from the ±2 ppm variation in the observation-based CO$_2$ profile at 2 km above sea level (**section 3.2**).

In all latitudes, obs. and satellite XCO$_2$ show an overall significant positive correlation (R^2: NIES = 0.84 ± 0.02, ACOS = 0.74 ± 0.08, OCO-2 = 0.82 ± 0.05) (**Table 2**). However, in the NH, satellite retrievals are negatively biased by up to 1.6 ± 0.6 ppm (ACOS) at 20° N–30° N (**Figs. 5a and 5d, Table 3**). The smallest average bias is found for NIES, likely due to the stricter quality filters as discussed in **section 4.1**. While ACOS and OCO-2 show rather a systematic offset, the NIES retrieval seems to be more noisy (**Figs. 5d and 5e, Table 3**). The root-mean-square error (RMSE) of the difference between obs. XCO$_2$ and satellite XCO$_2$ is 1.06, 1.26, and 1.70 for NIES, OCO-2, and ACOS respectively, and decreases by 40% (0.56 ppm) on average between the northernmost and southernmost regions (**Table 2**). Agreement within 1 ppm on average is found in the SH (**Figs. 5c and 5f**). The uncertainties of the differences between obs. XCO$_2$ and the satellite retrievals are large. However, the comparison indicates whether the results of the current satellite retrievals tend to show a systematic positive or negative offset (ACOS, OCO-2), or rather a random discrepancy. This comparison is of importance for revising the retrieval algorithm in future.
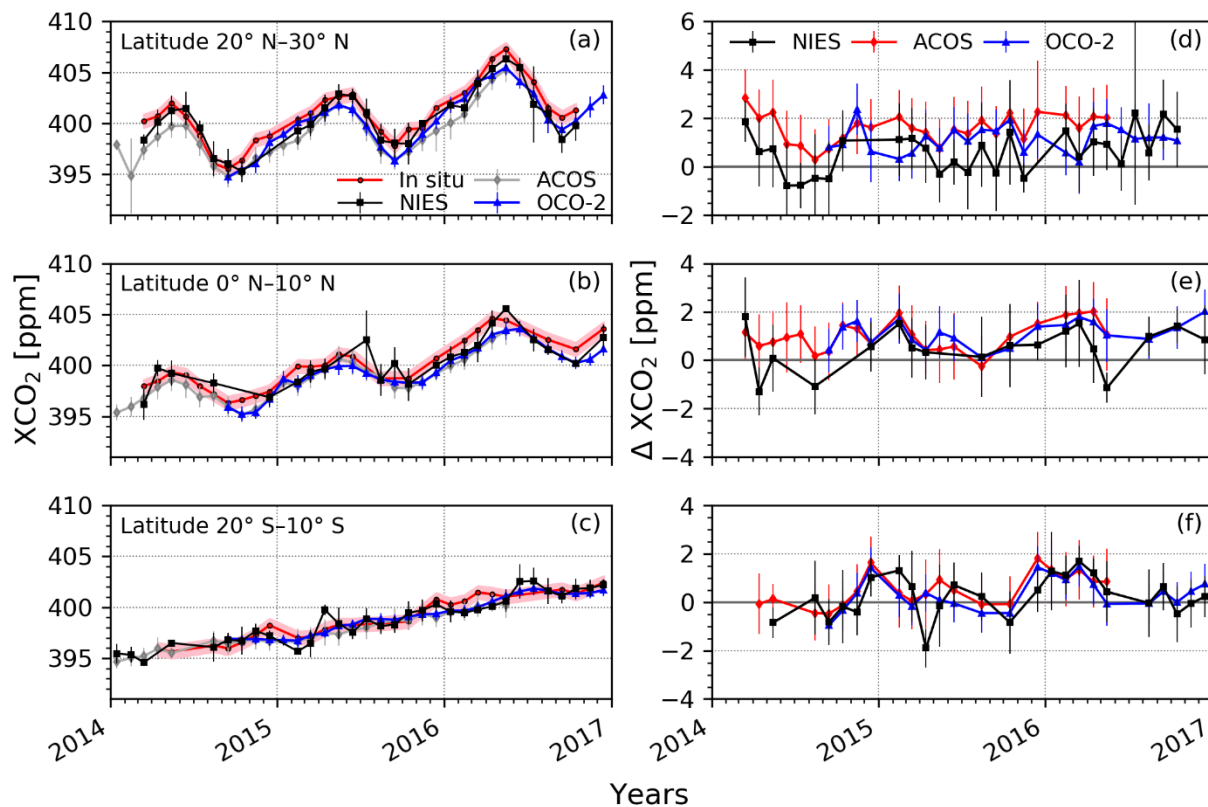
Figure 5. Temporal variation of the satellite derived XCO_2 obtained by NIES (black), ACOS (grey), and OCO-2 (blue) in comparison with the obs. XCO_2 (red) (left column), and the difference between obs. XCO_2 and NIES (black), ACOS (red), and OCO-2 (blue) (right column) for three selected latitude boxes. Red shaded areas are the uncertainty of the obs. XCO_2 derived from the ±2 ppm variability in the observation-based CO_2 profile at ~850 hPa. Error bars show the standard deviation of the monthly averaged XCO_2.

Table 2. Coefficient of determination (R^2) and root-mean-square error (RMSE) between obs. XCO_2 and satellite XCO_2 retrievals from GOSAT (NIES, ACOS) and OCO-2 at different latitude ranges between 2014 and 2017.

Latitude	R^2			RMSE		
	NIES	ACOS	OCO-2	NIES	ACOS	OCO-2
20° N–30° N	0.86	0.64	0.81	1.06	1.70	1.26
0° N–10° N	0.81	0.76	0.76	1.02	1.17	1.23
20° S–10° S	0.85	0.82	0.88	0.84	0.79	0.70

345

Table 3. Average (Avg.) difference and the standard deviation (SD.) between obs. and satellite XCO_2 from GOSAT (NIES, ACOS) and OCO-2 of each latitude range between 2014 and 2017.

	difference obs. XCO_2 – satellite XCO_2					
Latitude	**Avg. NIES**	**SD.**	**Avg. ACOS**	**SD.**	**Avg. OCO-2**	**SD.**
20° N–30° N	0.61	0.87	1.60	0.59	1.14	0.52
0° N–10° N	0.51	0.87	1.00	0.60	1.12	0.52
20° S–10° S	0.20	0.81	0.48	0.63	0.31	0.63

Figure 6 displays the latitudinal gradients and the gradient of the difference between obs. and satellite XCO_2 for the three selected months March, June, and October in 2015 as described above (**section 4.2**). It reveals that generally, the largest differences in the NH coincide with the latitude of the monthly XCO_2 maxima. Namely, at 30° N–40° N in spring and autumn with up to 3 ppm (between obs. XCO_2 and ACOS in March) (**Figs. 6a and 6d**) and in June at 10° N–20° N with a discrepancy of up to 2 ppm (between obs. XCO_2 and OCO-2) (**Figs. 6b and 6e**). The difference might be caused by uncertainties in the obs. XCO_2 due to the variability of the TROPPB (**section 3.2**). However, the uncertainty in the TROPPB results in a difference in the obs. XCO_2 of only 0.03 ± 0.06 ppm on average. This leads to a total estimated error of 0.7 ppm considering the uncertainty of 0.62 ± 0.01 ppm derived from the ± 2 ppm variation in the observation-based CO_2 profile at 2 km above sea level (**section 3.2**). It is known that atmospheric CO_2 mixing ratios in midlatitudes are characterized by high spatiotemporal variability. Therefore, the observed discrepancies in the NH may arise from differences in sample numbers, location and time within each month and latitude-longitude range. In particular, the largest uncertainty in the obs. XCO_2 likely results from the constructed CO_2 profile in the mid-troposphere, as no observational constraints are available for that part of the atmosphere and simply a linear interpolation between the ship and aircraft data was assumed (**section 3.2**).

However, **Fig. 3a** reveals that ship and aircraft CO_2 mixing ratios are very similar in the second half of each year. Model results of the MIROC4-ACTM confirm vertically uniform CO_2 profiles during that period, which lie within the uncertainty range of the observation-based profiles (**Fig. A3**). Niwa et al. (2011) found similar straight vertical profiles between June and September in East Asia, based on aircraft observations and model results. Furthermore, the maximum bias due to errors in the MIROC4-ACTM stratospheric CO_2 profile (0.9 ppm) is smaller than the average difference of 1.2 ± 0.4 ppm between the obs. XCO_2 and satellite observations of ACOS and OCO-2 between June and September (**section 3.2**). Hence, even though no assumption was necessary at that period, the negative bias persists (**Fig. 5d, Fig. 6e**), which indicates that the difference between obs. and satellite XCO_2 can be linked to measurement uncertainties of the satellites.
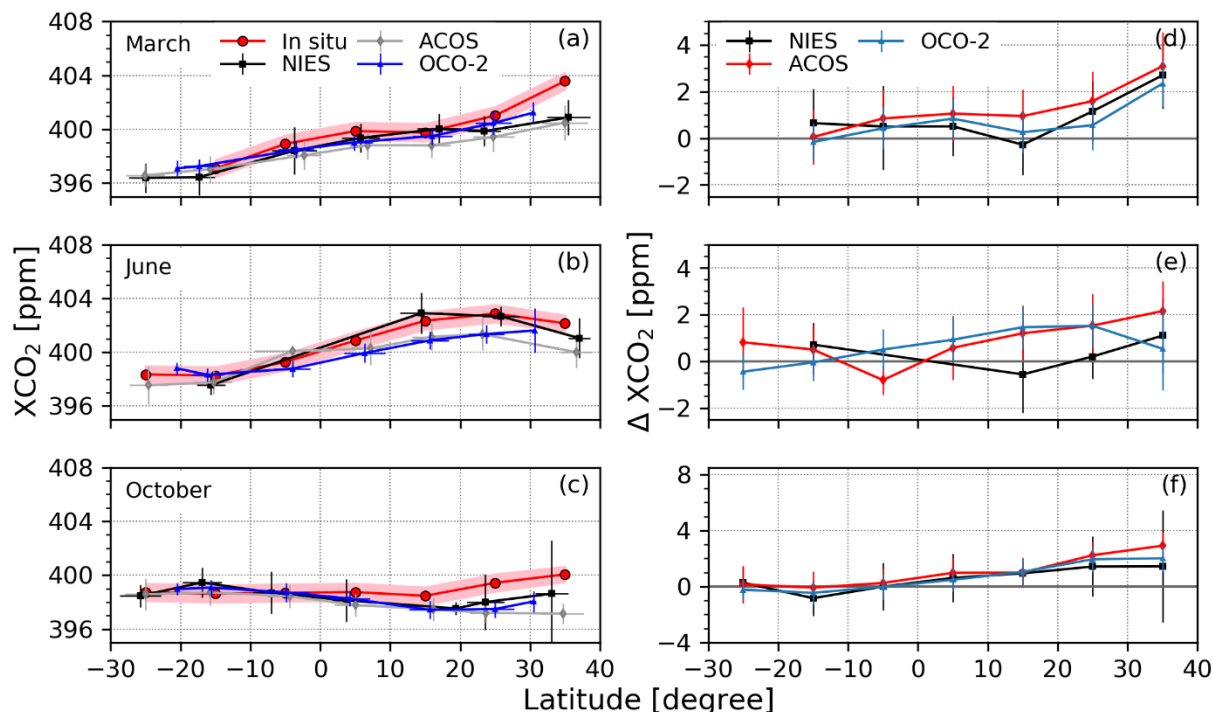
Figure 6. Latitudinal gradients of obs. XCO_2 (red) in comparison with the satellite XCO_2 from NIES (black), ACOS (grey), and OCO-2 (blue) (left column), and the difference between the obs. XCO_2 and NIES (black), ACOS (red), and OCO-2 (blue) (right column) for three selected months, March a) and d), June b) and e), and October c) and f) in 2015. Red shaded areas are the uncertainty of the obs. XCO_2 derived from the ±2 ppm variability in the observation-based CO_2 profile at ~850 hPa. Error bars show the standard deviation of the monthly averaged XCO_2 and of the location within each latitude box.

The peak values in the carbon cycle represent the turning points between predominant CO_2 sources in boreal winter, and sinks in summer and therefore, are important to constrain changes in the seasonal and interannual variation of the carbon cycle. **Figures 5a and 5b** reveal that maxima and minima generally agree. However, small positive phase shifts of about one month are occasionally observed (2014, 20° N–30° N: maximum of NIES in June; 2014, 10° N–20°N minima of ACOS and OCO-2 in October; 2016, 10° N–20°N: maximum of OCO-2 in June). Long-term measurements (1984 to 2013) observed maxima usually in May and minima in late September in the upper troposphere of the northern West Pacific (Matsueda et al., 2008, 2015). Surface data (between 1987 and 2017) reported maxima in early May and minima in early September over the same region (World Data Centre for Greenhouse Gases (WDCGG) of the World Meteorological Organization (WMO)). The consistency with long-term studies support the correctness of the obs. XCO_2, which implies that satellite XCO_2 sometimes show a delayed response to CO_2 changes, which might be caused by remaining uncertainties introduced by limitations in the retrieval algorithms and have not been previously identified due to the lack of validation data over the open ocean.

To explore year-to-year changes in the increase of XCO$_2$, the mean values of the three consecutive highest monthly averages
during spring of each year are compared (**Table 4**). Three-month averages around the peak values are chosen due to the limited
data, although usually longer time-periods are needed for that growth calculation. From 2014 to 2015, obs. and satellite XCO$_2$
increased by 1.61 ± 0.24 ppm yr^{-1} on average at 20° N–30° N **(Table 4, Fig. 5a)**. In contrast, a significant increase of
3.84 ± 0.65 ppm yr^{-1} is observed by obs. XCO$_2$ from 2015 to 2016. The average increase of the mean values of all satellite
retrievals is 3.39 ± 0.03 ppm yr^{-1}. This rapid increase is also seen near the equator, where the increase of the obs. XCO$_2$ is
significantly higher than that of ACOS and OCO-2 (two-sided t-test, significance level α=0.05). Simultaneously, a larger
negative bias of the satellite XCO$_2$ in 2016 as compared to the previous years is observed **(Figs. 5b and 5e)**.

Table 4. Increase of XCO$_2$ between peaks of consecutive years and the standard error of the difference seen by obs. and satellite XCO$_2$ of
GOSAT (NIES, ACOS) and OCO-2 between 2014 and 2017. Peak values are defined as mean of the three consecutive highest monthly
averages during spring of each year. In 2016, the mean of ACOS and that of obs. XCO$_2$ at 0° N–10° N is based on 2 months due to limited
data. "–" indicates missing data. The right column shows the average increase of all satellite means and its standard deviation.

	Obs. XCO$_2$ (ppm yr^{-1})	NIES (ppm yr^{-1})	ACOS (ppm yr^{-1})	OCO-2 (ppm yr^{-1})	Avg. all satellites (ppm yr^{-1})
			20° N–30° N		
2014–2015	1.45 ± 0.63	1.42 ± 0.60	1.95 ± 0.54	–	1.68 ± 0.26
2015–2016	3.84 ± 0.65	3.37 ± 0.43	3.43 ± 0.40	3.36 ± 0.38	3.39 ± 0.03
			0° N–10° N		
2014–2015	1.72 ± 0.22	–	1.99 ± 0.30	–	–
2015–2016	3.87 ± 0.09	–	2.82 ± 0.37	3.52 ± 0.16	3.17 ± 0.35

The larger increase between 2015 and 2016 is likely driven by the strong El Niño in 2015. Matsueda et al. (2008) reported a
mean CO$_2$ growth rate of 1.7 to 1.8 ppm yr^{-1} in 1993 to 2005. However, between 1997 to 1998, they found a significantly
enhanced growth rate of about 3 ppm yr^{-1}, which they linked to a strong El Niño year (Matsueda et al., 2002, 2008). Indeed,
it is well documented that the interannual variation in the growth rate of CO$_2$ is closely linked to the El Niño–Southern
Oscillation (ENSO), which affects the carbon cycle though changes in the atmospheric and ocean circulation (e.g., Bacastow,
1976; Keeling, C. D.Revelle, 1985; Kim et al., 2016; Patra et al., 2005; Wang et al., 2013; Zeng et al., 2005). Particularly, the
increase of CO$_2$ was attributed to a decrease in the NPP, increased soil respiration, and enhanced fire emissions related to low
precipitation and high temperatures (Liu et al., 2017). Recent model results found that the maximum CO$_2$ growth rate appears
several months after the El Niño peak as response to the low NPP (Kim et al., 2016). In fact, the maximum increase observed
in this study occurred in NH spring, after the peak of the 2015 El Niño in November/December **(Figs. 5a and 5b)**.

Opposite to the strong increase, obs. XCO$_2$ shows no increase between March and April around the equator in 2015 (**Fig. 5b**).
One month earlier (February), a reduction in XCO$_2$ is seen by ACOS and OCO-2. It has been argued that the upwelling of
carbon rich water to the surface at the equator is suppressed in the eastern and central Pacific Ocean during El Niño (Feely et

al., 2002; Keeling, C. D.Revelle, 1985), which subsequently leads to an initial negative CO_2 anomaly over that region (Rayner et al., 1999). Coincident timing of the observed anomalies with different phases of the El Niño suggest that the ocean and terrestrial response to the event affect the atmospheric CO_2 mixing ratio even at the study region at 140° E to 160° E. Supportive to this interpretation, Chatterjee et al. (2017) found a negative anomaly in atmospheric CO_2 concentrations over the so-called Niño 3.4 region (120° W–170° W) between March and July 2015 in the OCO-2 retrievals. Consequently, ACOS and OCO-2 reflect the negative anomaly of CO_2 of the first phase of the El Niño, whereas in the second phase, the response of the atmospheric CO_2 mixing ratio to the event is better represented by the higher growth rate of the obs. XCO_2. Given the uncertainties associated with the negative CO_2 anomaly observed at the study region, the result therefore suggests that, compared to satellite observations, obs. XCO_2 sometimes show a higher sensitivity to year-to-year changes in the atmospheric CO_2 mixing ratio.

5 Conclusions

The current study indicates that seasonal, latitudinal and interannual variation of atmospheric CO_2 mixing ratios over the open ocean can be accurately determined by observation-based column average CO_2 mixing ratios, defined as obs. XCO_2. The sensitivity of the obs. XCO_2 dataset to year-to-year variations was demonstrated on the distinct ocean and terrestrial responses to the 2015–2016 El Niño event around the equator. Namely, a stagnation in the springtime increase during the early stage of the El Niño event was linked to reduced CO_2 outgassing from the ocean, and a substantial increase to the later stage, reflecting the increase of CO_2 emissions from the terrestrial ecosystem.

The evaluation of three different satellite retrievals (ACOS, NIES, OCO-2) by the obs. XCO_2 revealed similar seasonal pattern ($R^2 = 0.64$–0.87). However, a negative bias of 1.12 ± 0.40 ppm on average and higher difference in the northern (NH) than in the southern hemisphere (SH) were attributed to measurement uncertainties of the satellites. Compared to ACOS and OCO-2, the NIES retrieval showed higher accuracy in the northern hemispherical midlatitudes. At low latitudes, NIES retrievals show substantial scatter and very few valid data points. ACOS and OCO-2 provide a more reliable analysis of carbon cycles at these latitudes. The seasonal cycle of all retrievals occasionally showed a positive phase shift of one month relative to the obs. XCO_2 at different times of year. In some cases, the representation of year-to-year variations in atmospheric CO_2 mixing ratios is more distinct in the obs. XCO_2 values as compared to the satellite estimates and therefore, are suggested to be sometimes of higher sensitivity. Hence, the result indicates that even if the retrievals complement each other, measurement uncertainties remain, which limit the accurate interpretation of spatiotemporal changes in CO_2 fluxes by satellites alone. These uncertainties might be introduced by limitations in the retrieval algorithms and have not been previously identified due to the lack of validation data over the open ocean.

Advanced observations like those from GOSAT-2 and improvements in retrieval algorithms like those from ACOS version 9, and OCO-2 version 10, increase the number of valid data points at lower latitudes and reduce uncertainties. An initial

comparison of the obs. XCO_2 dataset with ACOS v9 revealed a decrease of the negative bias by more than 50% on average as compared to ACOS v7.3 (**Fig. A1**), and the comparison with OCO-2 v10, a decrease of the average bias by more than 90% as compared to OCO-2 v9r (**Fig. A2**). This example highlights the utility of the obs. XCO_2 dataset as a reference for satellite derived XCO_2 estimates and to clarify the impacts of changes between different versions of retrieval algorithms.

450

Our study provides a short-term perspective on the great potential of the new bottom-up approach which can help to understand changes in the carbon cycle in response to global warming and to interpret their contribution to atmospheric CO_2 growth. We propose that a long-term XCO_2 dataset based on co-located CO_2 measurements by commercial ships and aircraft can augment TCCON data for validating XCO_2 estimates from satellites over the open ocean. To accomplish this objective, these commercial ship and aircraft measurements should be expanded and must be sustained for the foreseeable future.

455

Appendix A:
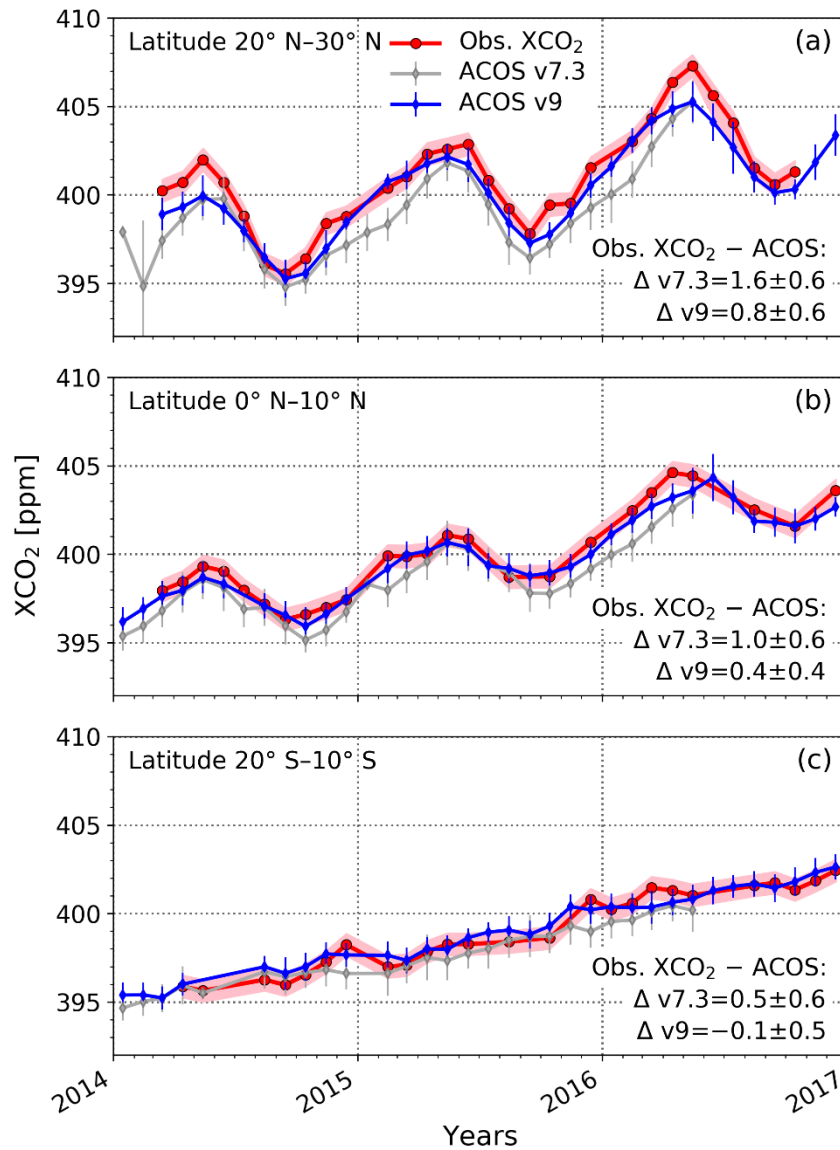
Figure A1. Comparison of the temporal variation of obs. XCO_2 (red) with XCO_2 derived from ACOS v7.3 (grey) and ACOS v9 (blue) for three selected latitude ranges. Red shaded areas are the uncertainty of the obs. XCO_2 derived from the ±2 ppm variability in the observation-based CO_2 profile at ~850 hPa. Error bars show the standard deviation of the monthly averaged XCO_2.

460
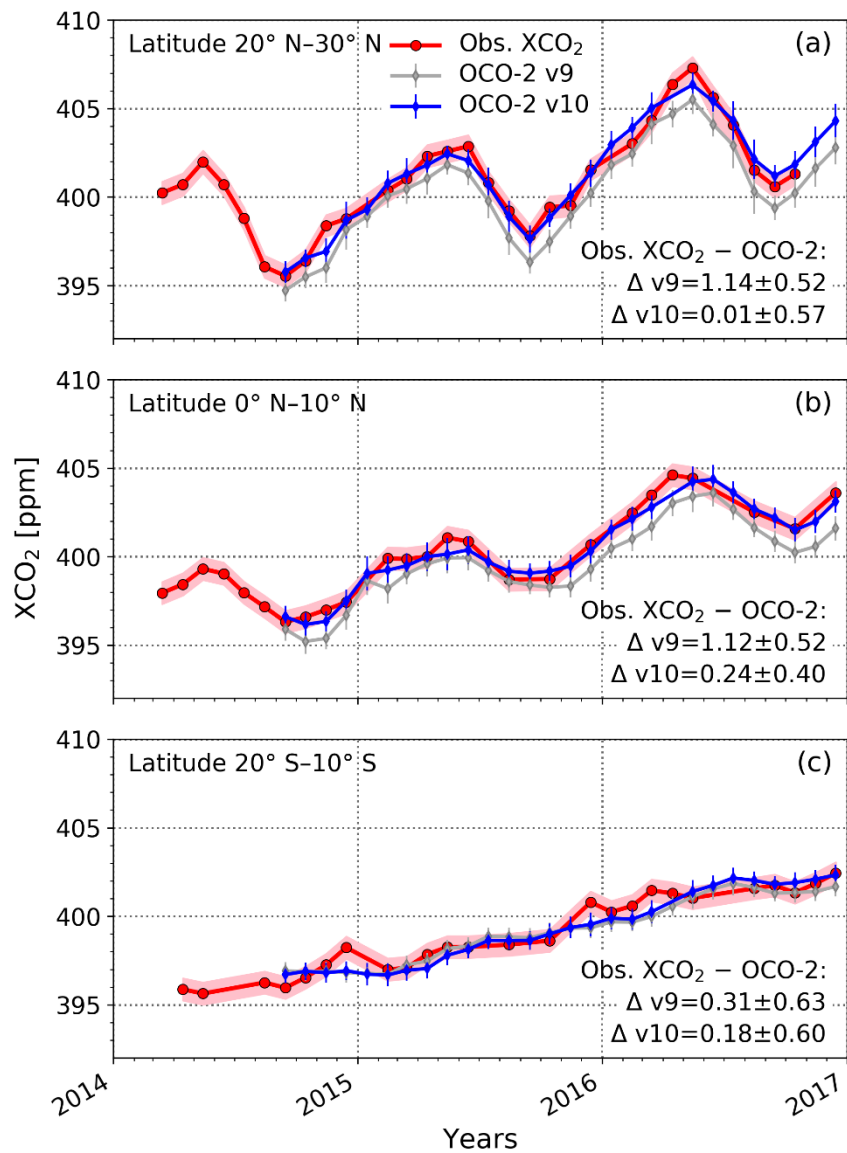
Figure A2. Comparison of the temporal variation of obs. XCO_2 (red) with XCO_2 derived from OCO-2 v9 (grey) and OCO-2 v10 (blue) for three selected latitude ranges. Red shaded areas are the uncertainty of the obs. XCO_2 which was obtained from the ±2 ppm variability in the observation-based CO_2 profile at ~850 hPa. Error bars show the standard deviation of the monthly averaged XCO_2.
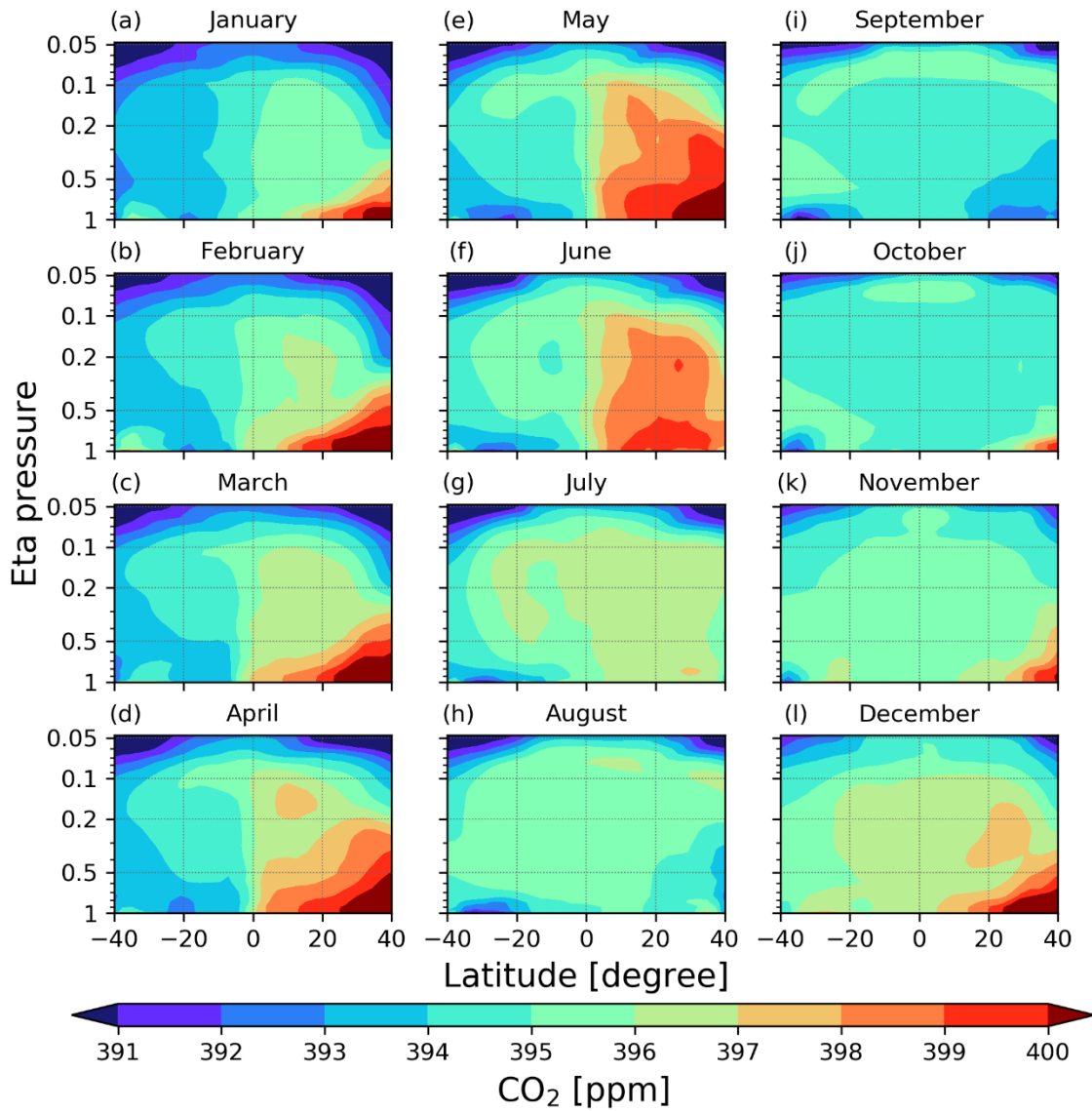
Figure A3. Latitude-pressure distribution of the inversion of the CO_2 mixing ratio at longitude 146° E in 2015, obtained from ACTM forward simulations.
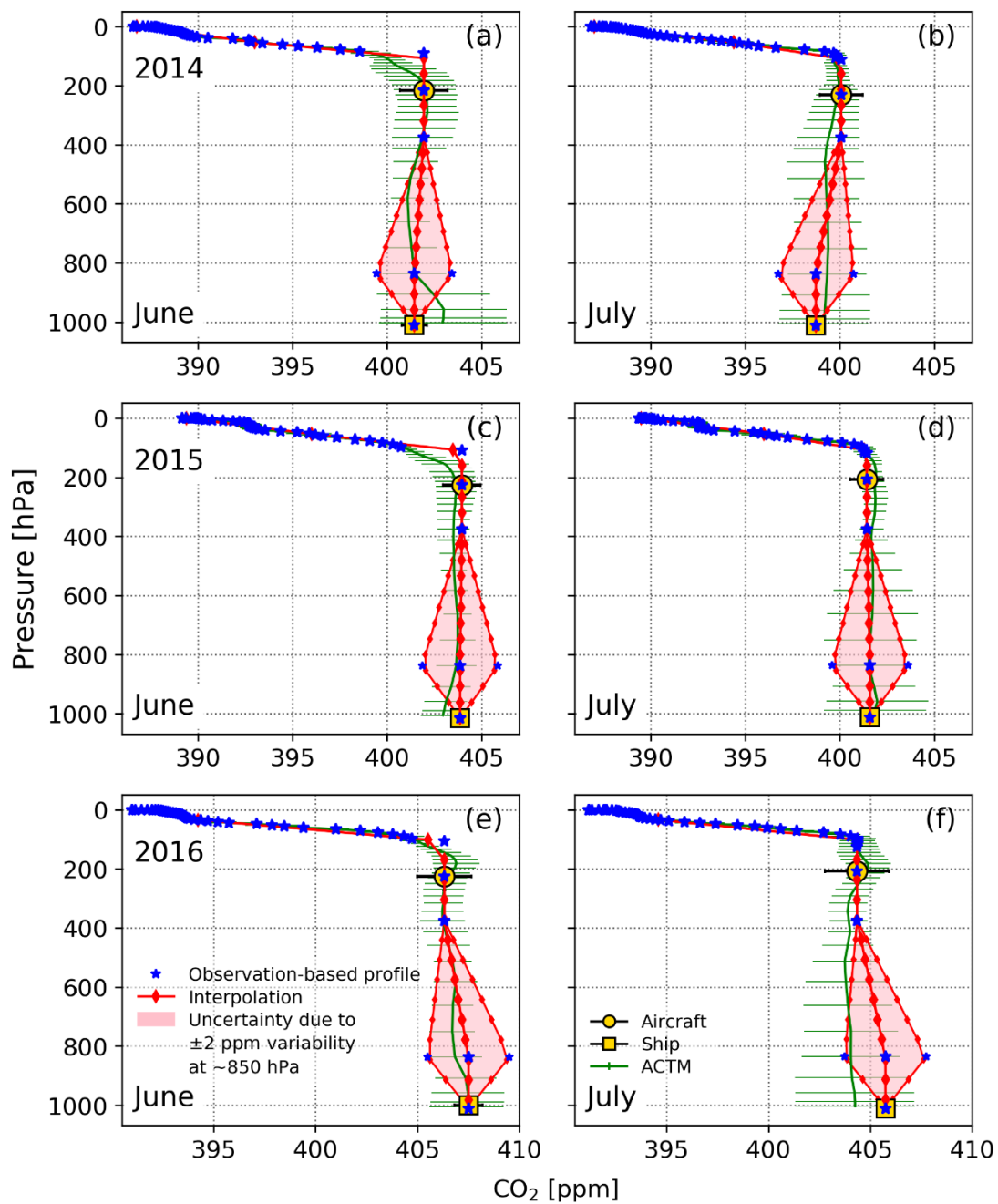
Figure A4. Observation-based CO_2 profiles (blue) obtained by using ship (SOOP) and aircraft (CONTRAIL) data (yellow), together with the results of the ACTM (green), and the interpolation (red) for the month June and July in 2014 a), b), 2015 c), d), and 2016 e), f) at the latitude range 20° N–30° N.

470

Data availability. The OCO-2 data presented in this manuscript are available from the NASA Goddard GES DISC at https://disc.gsfc.nasa.gov/datasets/OCO2_L2_Lite_FP_9r/summary (OCO-2 Science Team/Michael Gunson, Annmarie Eldering, 2018). ACOS data are available at https://disc.gsfc.nasa.gov/datasets/ACOS_L2_Lite_FP_9r/summary (OCO-2 Science Team/Michael Gunson, Annmarie Eldering, 2019), and at https://disc.gsfc.nasa.gov/datasets/ACOS_L2_Lite_FP_7.3/summary (OCO-2 Science Team/Michael Gunson, Annmarie Eldering, 2016). GOSAT data are available from the GOSAT Project website of the National Institute for Environmental Studies ("NIES") at https://data2.gosat.nies.go.jp/index_en.html, accessed: [4/28/2020]. SOOP data are available at http://soop.jp/, accessed: [9/26/2019]. The CONTRAIL CME CO_2 data are available on the Global Environmental Database of the Center for Global Environmental Studies of NIES (https://doi.org/10.17595/20180208.001). The CONTRAIL data are also available from the ObsPack data product (http://www.esrl.noaa.gov/gmd/ccgg/obspack/) and the World Data Center for Greenhouse Gases (https://gaw.kishou.go.jp/).

Supplementary data. Supplementary information and data accompany this article.

Author Contributions. The study was designed by H.T. Data analyses were made by A.M., and extensive discussions were made by A.M., H.T., T.S., T.M., P.P., J.L., and D.C. The paper was written, edited, and proofed by all the authors.

Competing Interests. The authors declare that they have no competing interests.

Acknowledgements. We are grateful to Dr. Naveen Chandra, NIES for providing CO_2 inversion fluxes that are used for simulating atmospheric concentration by ACTM. We also would like to thank the anonymous reviewers for valuable comments and suggestions improving the paper.

Financial support was given by multiple grants: the Global Environmental Research Coordination System from the Ministry of the Environment, Japan (E1851, E1253, E1652, E1151, E1951, E1451, E1751, E1432), and the Environmental Research and Technology Development Fund (ERTDF) from the Ministry of the Environment, Japan (grant no. 2-1803. JPMEERF20182003).

The authors acknowledge the satellite data infrastructure for providing access to the GOSAT NIES, the GOSAT ACOS and the OCO-2 data used in this study. This research is a contribution to the Research Announcement on GOSAT series joint research, entitled "Combined cargo-ship and passenger aircraft observations-based validation of GOSAT-2 GHG observations over the open oceans", and to the Greenhouse Gas Initiative of the Atmospheric Composition Virtual Constellation (AC-VC)

of the Committee on Earth Observation Satellites (CEOS). We thank the WDCGG (World Data Centre for Greenhouse Gases)
510 for providing CO_2 reference data of the Pacific Ocean from the NOAA GMD Carbon Cycle Cooperative Global Air Sampling
Network, 1968-2018 (Principal investigators include Ed Dlugokencky (NOAA)). Part of this work was conducted at the Jet
Propulsion Laboratory, California Institute of Technology, under contract to the National Aeronautics and Space
Administration. Government sponsorship acknowledged.

515

References

Bacastow, R. B.: Modulation of atmospheric carbon dioxide by the Southern Oscillation, Nature, 261(5556), 116–118, doi:10.1038/261116a0, 1976.

Basu, S., Guerlet, S., Butz, A., Houweling, S., Hasekamp, O., Aben, I., Krummel, P., Steele, P., Langenfelds, R., Torn, M.,
520 Biraud, S., Stephens, B., Andrews, A. and Worthy, D.: Global CO_2 fluxes estimated from GOSAT retrievals of total column CO_2, Atmos. Chem. Phys., 13(17), 8695–8717, doi:10.5194/acp-13-8695-2013, 2013.

Bisht, J. S. H., Machida, T., Chandra, N., Tsuboi, K., Patra, P. K., Umezawa, T., Niwa, Y., Sawa, Y., Morimoto, S., Nakazawa, T., Saitoh, N. and Takigawa, M.: Seasonal Variations of SF_6, CO_2, CH_4, and N_2O in the UT/LS Region due to Emissions, Transport, and Chemistry, J. Geophys. Res. Atmos., 126(4), 1–18, doi:10.1029/2020JD033541, 2021.

525 Canadell, J. G., Ciais, P., Gurney, K., Le Quéré, C., Piao, S., Raupach, M. R. and Sabine, C. L.: An International Effort to Quantify Regional Carbon Fluxes, Eos, Trans. Am. Geophys. Union, 92(10), 81–82, doi:10.1029/2011EO100001, 2011.

Chatterjee, A., Gierach, M. M., Sutton, A. J., Feely, R. A., Crisp, D., Eldering, A., Gunson, M. R., O'Dell, C. W., Stephens, B. B. and Schimel, D. S.: Influence of El Niño on atmospheric CO_2 over the tropical Pacific Ocean: Findings from NASA's OCO-2 mission, Science (80-.)., 358(6360), eaam5776, doi:10.1126/science.aam5776, 2017.

530 Chevallier, F., Ciais, P., Conway, T. J., Aalto, T., Anderson, B. E., Bousquet, P., Brunke, E. G., Ciattaglia, L., Esaki, Y., Fröhlich, M., Gomez, A., Gomez-Pelaez, A. J., Haszpra, L., Krummel, P. B., Langenfelds, R. L., Leuenberger, M., Machida, T., Maignan, F., Matsueda, H., Morguí, J. A., Mukai, H., Nakazawa, T., Peylin, P., Ramonet, M., Rivier, L., Sawa, Y., Schmidt, M., Steele, L. P., Vay, S. A., Vermeulen, A. T., Wofsy, S. and Worthy, D.: CO_2 surface fluxes at grid point scale estimated from a global 21 year reanalysis of atmospheric measurements, J. Geophys. Res., 115(D21),
535 D21307, doi:10.1029/2010JD013887, 2010.

Chevallier, F., Deutscher, N. M., Conway, T. J., Ciais, P., Ciattaglia, L., Dohe, S., Fröhlich, M., Gomez-Pelaez, A. J., Griffith, D., Hase, F., Haszpra, L., Krummel, P., Kyrö, E., Labuschagne, C., Langenfelds, R., Machida, T., Maignan, F., Matsueda, H., Morino, I., Notholt, J., Ramonet, M., Sawa, Y., Schmidt, M., Sherlock, V., Steele, P., Strong, K., Sussmann, R., Wennberg, P., Wofsy, S., Worthy, D., Wunch, D. and Zimnoch, M.: Global CO_2 fluxes inferred from surface air-sample
540 measurements and from TCCON retrievals of the CO_2 total column, Geophys. Res. Lett., 38(24), doi:10.1029/2011GL049899, 2011.

Connor, B. J., Boesch, H., Toon, G., Sen, B., Miller, C. and Crisp, D.: Orbiting Carbon Observatory: Inverse method and prospective error analysis, J. Geophys. Res. Atmos., 113(5), 1–14, doi:10.1029/2006JD008336, 2008.

Conway, T. J., Tans, P. P., Waterman, L. S., Thoning, K. W., Kitzis, D. R., Masarie, K. A. and Zhang, N.: Evidence for
545 interannual variability of the carbon cycle from the National Oceanic and Atmospheric Administration/Climate Monitoring and Diagnostics Laboratory Global Air Sampling Network, J. Geophys. Res., 99(D11), 22831, doi:10.1029/94JD01951, 1994.

Crisp, D., Fisher, B. M., O'Dell, C., Frankenberg, C., Basilio, R., Bösch, H., Brown, L. R., Castano, R., Connor, B., Deutscher, N. M., Eldering, A., Griffith, D., Gunson, M., Kuze, A., Mandrake, L., McDuffie, J., Messerschmidt, J., Miller, C. E., Morino, I., Natraj, V., Notholt, J., O'Brien, D. M., Oyafuso, F., Polonsky, I., Robinson, J., Salawitch, R., Sherlock, V., Smyth, M., Suto, H., Taylor, T. E., Thompson, D. R., Wennberg, P. O., Wunch, D. and Yung, Y. L.: The ACOS CO_2 retrieval algorithm - Part II: Global XCO_2 data characterization, Atmos. Meas. Tech., 5(4), 687–707, doi:10.5194/amt-5-687-2012, 2012.

Crisp, D., Pollock, H., Rosenberg, R., Chapsky, L., Lee, R., Oyafuso, F., Frankenberg, C., Dell, C., Bruegge, C., Doran, G., Eldering, A., Fisher, B., Fu, D., Gunson, M., Mandrake, L., Osterman, G., Schwandner, F., Sun, K., Taylor, T., Wennberg, P. and Wunch, D.: The on-orbit performance of the Orbiting Carbon Observatory-2 (OCO-2) instrument and its radiometrically calibrated products, Atmos. Meas. Tech., 10(1), 59–81, doi:10.5194/amt-10-59-2017, 2017.

Crowell, S., Baker, D., Schuh, A., Basu, S., Jacobson, A. R., Chevallier, F., Liu, J., Deng, F., Feng, L., McKain, K., Chatterjee, A., Miller, J. B., Stephens, B. B., Eldering, A., Crisp, D., Schimel, D., Nassar, R., O'Dell, C. W., Oda, T., Sweeney, C., Palmer, P. I. and Jones, D. B. A.: The 2015–2016 carbon cycle as seen from OCO-2 and the global in situ network, Atmos. Chem. Phys., 19(15), 9797–9831, doi:10.5194/acp-19-9797-2019, 2019.

Dlugokencky, E. and Tans, P.: Trends in Atmospheric Carbon Dioxide, NOAA/GML; www.esrl.noaa.gov/gmd/ccgg/trends/, last access: 7 January 2021.

Feely, R. A., Boutin, J., Cosca, C. E., Dandonneau, Y., Etcheto, J., Inoue, H. Y., Ishii, M., Quéré, C. Le, Mackey, D. J., McPhaden, M., Metzl, N., Poisson, A. and Wanninkhof, R.: Seasonal and interannual variability of CO_2 in the equatorial Pacific, Deep. Res. Part II Top. Stud. Oceanogr., 49(13–14), 2443–2469, doi:10.1016/S0967-0645(02)00044-9, 2002.

Frankenberg, C., Kulawik, S. S., Wofsy, S. C., Chevallier, F., Daube, B., Kort, E. A., O'Dell, C., Olsen, E. T. and Osterman, G.: Using airborne HIAPER pole-to-pole observations (HIPPO) to evaluate model and remote sensing estimates of atmospheric carbon dioxide, Atmos. Chem. Phys., 16(12), 7867–7878, doi:10.5194/acp-16-7867-2016, 2016.

Friedlingstein, P., Jones, M. W., O'Sullivan, M., Andrew, R. M., Hauck, J., Peters, G. P., Peters, W., Pongratz, J., Sitch, S., Le Quéré, C., Bakker, D. C. E., Canadell, J. G., Ciais, P., Jackson, R. B., Anthoni, P., Barbero, L., Bastos, A., Bastrikov, V., Becker, M., Bopp, L., Buitenhuis, E., Chandra, N., Chevallier, F., Chini, L. P., Currie, K. I., Feely, R. A., Gehlen, M., Gilfillan, D., Gkritzalis, T., Goll, D. S., Gruber, N., Gutekunst, S., Harris, I., Haverd, V., Houghton, R. A., Hurtt, G., Ilyina, T., Jain, A. K., Joetzjer, E., Kaplan, J. O., Kato, E., Klein Goldewijk, K., Korsbakken, J. I., Landschützer, P., Lauvset, S. K., Lefèvre, N., Lenton, A., Lienert, S., Lombardozzi, D., Marland, G., McGuire, P. C., Melton, J. R., Metzl, N., Munro, D. R., Nabel, J. E. M. S., Nakaoka, S.-I., Neill, C., Omar, A. M., Ono, T., Peregon, A., Pierrot, D., Poulter, B., Rehder, G., Resplandy, L., Robertson, E., Rödenbeck, C., Séférian, R., Schwinger, J., Smith, N., Tans, P. P., Tian, H., Tilbrook, B., Tubiello, F. N., van der Werf, G. R., Wiltshire, A. J. and Zaehle, S.: Global Carbon Budget 2019, Earth Syst. Sci. Data, 11(4), 1783–1838, doi:10.5194/essd-11-1783-2019, 2019.

Hakkarainen, J., Ialongo, I., Maksyutov, S. and Crisp, D.: Analysis of Four Years of Global XCO_2 Anomalies as Seen by Orbiting Carbon Observatory-2, Remote Sens., 11(7), 850, doi:10.3390/rs11070850, 2019.

Inai, Y., Aoki, S., Honda, H., Furutani, H., Matsumi, Y., Ouchi, M., Sugawara, S., Hasebe, F., Uematsu, M. and Fujiwara, M.: Balloon-borne tropospheric CO_2 observations over the equatorial eastern and western Pacific, Atmos. Environ., 184(December 2017), 24–36, doi:10.1016/j.atmosenv.2018.04.016, 2018.

Inoue, M., Morino, I., Uchino, O., Miyamoto, Y., Yoshida, Y., Yokota, T., Machida, T., Sawa, Y., Matsueda, H., Sweeney, C., Tans, P. P., Andrews, A. E., Biraud, S. C., Tanaka, T., Kawakami, S. and Patra, P. K.: Validation of XCO_2 derived from SWIR spectra of GOSAT TANSO-FTS with aircraft measurement data, Atmos. Chem. Phys, 13, 9771–9788, doi:10.5194/acp-13-9771-2013, 2013.

Intergovernmental Panel on Climate Change (IPCC): Climate Change 2013 - The Physical Science Basis, edited by Intergovernmental Panel on Climate Change, Cambridge University Press, Cambridge., 2013.

Keeling, C. D.Revelle, R.: Effects of El Nino/Southern Oscillation on the Atmospheric Content of Carbon Dioxide, Meteoritics, 20(2), 437–450, 1985.

Kim, J. S., Kug, J. S., Yoon, J. H. and Jeong, S. J.: Increased atmospheric CO_2 growth rate during El Niño driven by reduced terrestrial productivity in the CMIP5 ESMs, J. Clim., 29(24), 8783–8805, doi:10.1175/JCLI-D-14-00672.1, 2016.

595 Kobayashi, S., Ota, Y., Harada, Y., Ebita, A., Moriya, M., Onoda, H., Onogi, K., Kamahori, H., Kobayashi, C., Endo, H., Miyaoka, K. and Takahashi, K.: The JRA-55 Reanalysis: General Specifications and Basic Characteristics, J. Meteorol. Soc. Japan. Ser. II, 93(1), 5–48, doi:10.2151/jmsj.2015-001, 2015.

Kulawik, S. S., Crowell, S., Baker, D., Liu, J., Mckain, K., Sweeney, C., Biraud, S. C., Wofsy, S., Dell, C. W. O., Wennberg, P. O., Wunch, D., Roehl, M., Deutscher, N. M., Kiel, M., Griffith, D. W. T., Velazco, V. A., Dubey, M. K., Sepulveda, 600 E., Elena, O., Rodriguez, G., Té, Y., Heikkinen, P., Dlugokencky, E. J., Gunson, M. R., Eldering, A., Fisher, B. and Osterman, G. B.: Characterization of OCO-2 and ACOS-GOSAT biases and errors for CO_2 flux estimates, (October), 2019.

Kuze, A., Suto, H., Nakajima, M. and Hamazaki, T.: Thermal and near infrared sensor for carbon observation Fourier-transform spectrometer on the Greenhouse Gases Observing Satellite for greenhouse gases monitoring, Appl. Opt., 605 48(35), 6716, doi:10.1364/AO.48.006716, 2009.

Laughner, J., Andrews, A., Roche, S., Kiel, M. and Toon, G.: ginput v1.0.7b: GGG2020 prior profile software, CaltechDATA., 2021.

Laughner, J.L.; Kiel, M.; Toon, G.; Andrews, A.; Roche, S.; Wunch, D.; Wennberg, P.O. (in prep). Revised formulation of the TCCON priors for GGG2020.

610 Liu, J., Bowman, K. W., Schimel, D. S., Parazoo, N. C., Jiang, Z., Lee, M., Bloom, A. A., Wunch, D., Frankenberg, C., Sun, Y., O'Dell, C. W., Gurney, K. R., Menemenlis, D., Gierach, M., Crisp, D. and Eldering, A.: Contrasting carbon cycle responses of the tropical continents to the 2015–2016 El Niño, Science (80-.)., 358(6360), doi:10.1126/science.aam5690, 2017.

Machida, T., Matsueda, H., Sawa, Y., Nakagawa, Y., Hirotani, K., Kondo, N., Goto, K., Nakazawa, T., Ishikawa, K. and 615 Ogawa, T.: Worldwide measurements of atmospheric CO_2 and other trace gas species using commercial airlines, J. Atmos. Ocean. Technol., 25(10), 1744–1754, doi:10.1175/2008JTECHA1082.1, 2008.

Matsueda, H., Inoue, H. Y. and Ishii, M.: Aircraft observation of carbon dioxide at 8-13 km altitude over the Western Pacific from 1993 to 1999, Tellus, Ser. B Chem. Phys. Meteorol., 54(1), 1–21, doi:10.1034/j.1600-0889.2002.00304.x, 2002.

Matsueda, H., Machida, T., Sawa, Y., Nakagawa, Y., Hirotani, K., Ikeda, H., Kondo, N. and Goto, K.: Evaluation of 620 atmospheric CO_2 measurements from new flask air sampling of JAL airliner observations, Pap. Meteorol. Geophys., 59(March), 1–17, doi:10.2467/mripapers.59.1, 2008.

Matsueda, H., Machida, T., Sawa, Y. and Niwa, Y.: Long-term change of CO_2 latitudinal distribution in the upper troposphere, Geophys. Res. Lett., 42(7), 2508–2514, doi:10.1002/2014GL062768, 2015.

Miller, C. E., Crisp, D., DeCola, P. L., Olsen, S. C., Randerson, J. T., Michalak, A. M., Alkhaled, A., Rayner, P., Jacob, D. J., 625 Suntharalingam, P., Jones, D. B. A., Denning, A. S., Nicholls, M. E., Doney, S. C., Pawson, S., Boesch, H., Connor, B. J., Fung, I. Y., O'Brien, D., Salawitch, R. J., Sander, S. P., Sen, B., Tans, P., Toon, G. C., Wennberg, P. O., Wofsy, S. C., Yung, Y. L. and Law, R. M.: Precision requirements for space-based data, J. Geophys. Res. Atmos., 112(D10), 1–19, doi:10.1029/2006JD007659, 2007.

Miyazaki, K., Patra, P. K., Takigawa, M., Iwasaki, T. and Nakazawa, T.: Global-scale transport of carbon dioxide in the 630 troposphere, J. Geophys. Res. Atmos., 113(15), 1–21, doi: 10.1029/2007JD009557, 2008.

Morino, I., Tsutsumi, Y., Uchino, O., Ohyama, H., Thi Ngoc Trieu, T., Frey, M. M., Yoshida, Y., Matsunaga, T., Kamei, A., Saito, M. and Noda, H. M.: Status of GOSAT and GOSAT-2 FTS SWIR L2 Product Validation, in The 16th International Workshop on Greenhouse Gas Measurement from Space, pp. 2–5., 2020.

635 Nakajima, M., Suto, H., Yotsumoto, K., Shiomi, K. and Hirabayashi, T.: Fourier transform spectrometer on GOSAT and GOSAT-2, in International Conference on Space Optics — ICSO 2014, vol. 10563, edited by B. Cugny, Z. Sodnik, and N. Karafolas, p. 2, SPIE., 2017.

Nakazawa, T., MIYASHITA, K., AOKI, S. and TANAKA, M.: Temporal and spatial variations of upper tropospheric and lower stratospheric carbon dioxide, Tellus B, 43(2), 106–117, doi:10.1034/j.1600-0889.1991.t01-1-00005.x, 1991.

640 Niwa, Y., Patra, P. K., Sawa, Y., MacHida, T., Matsueda, H., Belikov, D., Maki, T., Ikegami, M., Imasu, R., Maksyutov, S., Oda, T., Satoh, M. and Takigawa, M.: Three-dimensional variations of atmospheric CO_2: Aircraft measurements and multi-transport model simulations, Atmos. Chem. Phys., 11(24), 13359–13375, doi:10.5194/acp-11-13359-2011, 2011.

O'Dell, C. W., Connor, B., Bösch, H., O'Brien, D., Frankenberg, C., Castano, R., Christi, M., Eldering, D., Fisher, B., Gunson, M., McDuffie, J., Miller, C. E., Natraj, V., Oyafuso, F., Polonsky, I., Smyth, M., Taylor, T., Toon, G. C., Wennberg, P. O. and Wunch, D.: The ACOS CO_2 retrieval algorithm-Part 1: Description and validation against synthetic observations, 645 Atmos. Meas. Tech., 5(1), 99–121, doi:10.5194/amt-5-99-2012, 2012.

OCO-2 Science Team/Michael Gunson, Annmarie Eldering, 2016. ACOS GOSAT/TANSO-FTS Level 2 bias-corrected XCO_2 and other select fields from the full-physics retrieval aggregated as daily files V7.3. Greenbelt, MD, USA, Goddard Earth Sciences Data and Information Services Center (GES DISC). https://disc.gsfc.nasa.gov/datacollection/ACOS_L2_Lite_FP_7.3.html. Accessed: [4/16/2020].

650 OCO-2 Science Team/Michael Gunson, Annmarie Eldering, 2018. OCO-2 Level 2 bias-corrected XCO2 and other select fields from the full-physics retrieval aggregated as daily files, Retrospective processing V9r. Greenbelt, MD, USA, Goddard Earth Sciences Data and Information Services Center (GES DISC). https://doi.org/10.5067/W8QGIYNKS3JC. Accessed: [5/7/2020].

OCO-2 Science Team/Michael Gunson, Annmarie Eldering, 2019. ACOS GOSAT/TANSO-FTS Level 2 bias-corrected XCO_2 655 and other select fields from the full-physics retrieval aggregated as daily files V9r. Greenbelt, MD, USA, Goddard Earth Sciences Data and Information Services Center (GES DISC). https://doi.org/10.5067/VWSABTO7ZII4. Accessed: [8/7/2020].

Patra, P. K., Maksyutov, S., Sasano, Y., Nakajima, H., Inoue, G. and Nakazawa, T.: An evaluation of CO_2 observations with Solar Occultation FTS for Inclined-Orbit Satellite sensor for surface source inversion, J. Geophys. Res. Atmos., 660 108(D24), n/a-n/a, doi:10.1029/2003JD003661, 2003.

Patra, P. K., Ishizawa, M., Maksyutov, S., Nakazawa, T. and Inoue, G.: Role of biomass burning and climate anomalies for land-atmosphere carbon fluxes based on inverse modeling of atmospheric CO_2, Global Biogeochem. Cycles, 19(3), 1–10, doi:10.1029/2004GB002258, 2005.

Patra, P. K., Takigawa, M., Watanabe, S., Chandra, N., Ishijima, K. and Yamashita, Y.: Improved chemical tracer simulation 665 by MIROC4.0-based atmospheric chemistry-transport model (MIROC4-ACTM), Sci. Online Lett. Atmos., 14, 91–96, doi:10.2151/SOLA.2018-016, 2018.

Rayner, P. J., Law, R. M. and Dargaville, R.: The relationship between tropical CO_2 fluxes and the El Niño-Southern Oscillation, Geophys. Res. Lett., 26(4), 493–496, doi:10.1029/1999GL900008, 1999.

Reuter, M., Bösch, H., Bovensmann, H., Bril, A., Buchwitz, M., Butz, A., Burrows, J. P., O'Dell, C. W., Guerlet, S., Hasekamp, 670 O., Heymann, J., Kikuchi, N., Oshchepkov, S., Parker, R., Pfeifer, S., Schneising, O., Yokota, T. and Yoshida, Y.: A joint effort to deliver satellite retrieved atmospheric CO_2 concentrations for surface flux inversions: the ensemble median algorithm EMMA, Atmos. Chem. Phys., 13(4), 1771–1780, doi:10.5194/acp-13-1771-2013, 2013.

Sawa, Y., Machida, T. and Matsueda, H.: Aircraft observation of the seasonal variation in the transport of CO_2 in the upper atmosphere, J. Geophys. Res. Atmos., 117(D5), doi:10.1029/2011JD016933, 2012.

675 Umezawa, T., Matsueda, H., Sawa, Y., Niwa, Y., Machida, T. and Zhou, L.: Seasonal evaluation of tropospheric CO_2 over the Asia-Pacific region observed by the CONTRAIL commercial airliner measurements, Atmos. Chem. Phys., 18(20), 14851–14866, doi:10.5194/acp-18-14851-2018, 2018.

Velazco, V. A., Morino, I., Uchino, O., Hori, A., Kiel, M., Bukosa, B., Deutscher, N. M., Sakai, T., Nagai, T., Bagtasa, G., Izumi, T., Yoshida, Y. and Griffith, D. W. T.: TCCON Philippines: First measurement results, satellite data and model comparisons in Southeast Asia, Remote Sens., 9(12), 1–18, doi:10.3390/rs9121228, 2017.

Wang, W., Ciais, P., Nemani, R. R., Canadell, J. G., Piao, S., Sitch, S., White, M. A., Hashimoto, H., Milesi, C. and Myneni, R. B.: Variations in atmospheric CO_2 growth rates coupled with tropical temperature (Proceedings of the National Academy of Sciences of the United States of America (2013) 110, 32 (13061-13066) DOI:10.1073/pnas.1219683110), Proc. Natl. Acad. Sci. U. S. A., 110(37), 15163, doi:10.1073/pnas.1314920110, 2013.

Wilcox, L. J., Hoskins, B. J. and Shine, K. P.: A global blended tropopause based on ERA data. Part I: Climatology, Q. J. R. Meteorol. Soc., 138(664), 561–575, doi:10.1002/qj.951, 2012.

Wofsy, S. C.: HIAPER Pole-to-Pole Observations (HIPPO): fine-grained, global-scale measurements of climatically important atmospheric gases and aerosols, Philos. Trans. R. Soc. A Math. Phys. Eng. Sci., 369(1943), 2073–2086, doi:10.1098/rsta.2010.0313, 2011.

Wofsy, S. C., Afshar, S., Allen, H. M., Apel, E., Asher, E. C., Barletta, B., Bent, J., Bian, H., Biggs, B. C., Blake, D. R., Blake, N., Bourgois, I., Brock, C. A., Brune, W. H., Budney, J. W., Bui, T. P., Butler, A., Campuzano-Jost, P., Chang, C. S., Chin, M., Commane, R., Correa, G., Crounse, J. D., Cullis, P. D., Daube, B. C., Day, D. A., Dean-Day, J. M., Dibb, J. E., Digangi, J. P., Diskin, G. S., Dollner, M., Elkins, J. W., Erdesz, F., Fiore, A. M., Flynn, C. M., Froyd, K., Gesler, D. W., Hall, S. R., Hanisco, T. F., Hannun, R. A., Hills, A. J., Hintsa, E. J., Hoffmann, A., Hornbrook, R. S., Huey, L. G., Hughes, S., Jimenez, J. L., Johnson, B. J., Katich, J. M., Keeling, R., Kim, M. J., Kupc, A., Lait, L. R., Lamarque, J.-F., Liu, H. B., McKain, K., Mclaughlin, R. J., Meinardi, S., Miller, D. O., Montzka, S. A., Moore, F. L., Morgan, E. J., Murphy, D. M., Murray, L. T., Nault, B. A., Neuman, J. A., Newman, P. A., Nicely, J. M., Pan, X., Paplawsky, W., Peischl, J., Prather, M. J., Price, D. J., Ray, E., Reeves, J. M., Richardson, M., Rollins, A. W., Rosenlof, K. H., Ryerson, T. B., Scheuer, E., Schill, G. P., Schroder, J. C., Schwarz, J. P., St.Clair, J. M., Steenrod, S. D., Stephens, B. B., Strode, S. A., Sweeney, C., Tanner, D., Teng, A. P., Thames, A. B., Thompson, C. R., Ullmann, K., Veres, P. R., Vizenor, N., Wagner, N. L., Watt, A., Weber, R., Weinzierl, B., et al.: ATom: Merged Atmospheric Chemistry, Trace Gases, and Aerosols, , doi:10.3334/ORNLDAAC/1581, 2018.

Wunch, D., Toon, G. C., Blavier, J.-F. L., Washenfelder, R. A., Notholt, J., Connor, B. J., Griffith, D. W. T., Sherlock, V. and Wennberg, P. O.: The Total Carbon Column Observing Network, Philos. Trans. R. Soc. A Math. Phys. Eng. Sci., 369(1943), 2087–2112, doi:10.1098/rsta.2010.0240, 2011.

Yamagishi, H., Tohjima, Y., Mukai, H., Nojiri, Y., Miyazaki, C. and Katsumata, K.: Observation of atmospheric oxygen/nitrogen ratio aboard a cargo ship using gas chromatography/thermal conductivity detector, J. Geophys. Res. Atmos., 117(D4), doi:10.1029/2011JD016939, 2012.

Yoshida, Y., Kikuchi, N., Morino, I., Uchino, O., Oshchepkov, S., Bril, A., Saeki, T., Schutgens, N., Toon, G. C., Wunch, D., Roehl, C. M., Wennberg, P. O., Griffith, D. W. T., Deutscher, N. M., Warneke, T., Notholt, J., Robinson, J., Sherlock, V., Connor, B., Rettinger, M., Sussmann, R., Ahonen, P., Heikkinen, P., Kyrö, E., Mendonca, J., Strong, K., Hase, F., Dohe, S. and Yokota, T.: Improvement of the retrieval algorithm for GOSAT SWIR XCO_2 and XCH_4 and their validation using TCCON data, Atmos. Meas. Tech., 6(6), 1533–1547, doi:10.5194/amt-6-1533-2013, 2013.

Zeng, N., Mariotti, A. and Wetzel, P.: Terrestrial mechanisms of interannual CO_2 variability, Global Biogeochem. Cycles, 19(1), 1–15, doi:10.1029/2004GB002273, 2005.